Precipitation Hydrometeor Type Relative to the Mesoscale Airflow in Mature Oceanic Deep Convection of the Madden-Julian Oscillation

Hannah C. Barnes and Robert A. Houze, Jr.

Department of Atmospheric Sciences, University of Washington, Seattle, Washington, USA

Corresponding author: H. C. Barnes, Department of Atmospheric Sciences, University of Washington, Box 351640, Seattle, WA 98195 (hannah@atmos.washington.edu)

Submitted to *Journal of the Geophysical Research – Atmospheres*

Submitted: 27 June 2014

Revised: 2 October 2014

Key Points

- Hydrometeor types are systematically located relative to mesoscale air motions
- Heavy rain and riming occur downstream of mesoscale convective updrafts
- Pockets of rimed ice particles occur near melting level in stratiform region

Abstract

Composite analysis of mature near-equatorial oceanic mesoscale convective systems (MCSs) during the active stage of the Madden-Julian Oscillation (MJO) show where different hydrometeor types occur relative to convective updraft and stratiform midlevel inflow layers. The National Center for Atmospheric Research (NCAR) S-PolKa radar observed these MCSs during the Dynamics of the Madden-Julian Oscillation/Atmospheric Radiation Measurement-MJO Investigation Experiment (DYNAMO/AMIE). NCAR's particle identification algorithm (PID) is applied to S-PolKa's polarimetric data to identify the dominant hydrometeor type in each radar sample volume. Combining S-PolKa's Doppler-velocity data with the PID demonstrates that hydrometeors have a systematic relationship to the airflow within mature MCSs. In the convective region: moderate rain occurs within the updraft core; the heaviest rain occurs just downwind of the core; wet aggregates occur immediately below the melting layer; narrow zones containing graupel/rimed aggregates occur just downstream of the updraft core at midlevels; dry aggregates dominate above the melting level; and smaller ice particles occur along the edges of the convective zone. In the stratiform region: rain intensity decreases towards the anvil; melting aggregates occur in horizontally extensive but vertically thin regions at the

melting layer; intermittent pockets of graupel/rimed aggregates occur atop the melting layer; dry aggregates and small ice particles occur sequentially above the melting level; horizontally-oriented ice crystals occur between –10°C to –20°C in turbulent air above the descending midlevel inflow, suggesting enhanced depositional growth of dendrites. The organization of hydrometeors within the midlevel inflow layer is insensitive to the presence or absence of a leading convective line.

Index Terms and Keywords

AGU: 3329 Mesoscale Meteorology, 3371 Tropical Convection, 9340 Indian Ocean

Author Key Words: Mesoscale Convective Systems, dual-polarimetric radar, hydrometeors, Madden-Julian Oscillation, microphysical processes

Text

1. Introduction

Mesoscale convective systems (MCSs) are broadly defined as cloud systems whose contiguous precipitation spans at least ~100 km in one direction [*Houze,* 2004]. These cloud systems are comprised of small, intensely precipitating convective regions and expansive stratiform regions that have a relatively steady but reduced precipitation rate. If the convective

cells are organized into a line ahead of a moving stratiform region, the MCS is referred to as a stratiform region with a leading-convective line. The leading line is commonly called a squall line. If the convective cells are embedded within the MCS, the storm is said to contain a stratiform region without a leading-convective line. *Leary and Houze* [1979a] and *Houze and Betts* [1981] referred to these two types of MCSs as "squall clusters" and "non-squall clusters." The convective and stratiform portions of MCSs are also characterized by distinct kinematic structures. Using an idealized, steady state two-dimensional numerical simulation with prescribed environmental instability and vertical wind shear, *Moncrieff* [1992] suggested that air moves through an MCS in coherent layers. *Kingsmill and Houze* [1999a] confirmed this layered airflow through a dual-Doppler analysis of airborne radar data obtained during the Tropical Ocean Global Atmosphere Coupled Ocean Atmosphere Response Experiment (TOGA COARE) in the west Pacific Ocean. Their results indicate that mature convective regions are characterized by a relatively deep surface convergent layer that steeply rises until it diverges near cloud top. Mature stratiform regions are distinguished by a midlevel inflow layer that converges beneath the anvil and gradually slopes downwards toward the center of the MCS. An upper-level mesoscale sloping updraft layer is located above the midlevel inflow layer.

These airflow patterns influence various aspects of the storm, including microphysical processes and the locations of different types of hydrometeors in three-dimensional space. More rapidly falling, denser hydrometeors reach the surface much closer to the convective updraft core. More slowly falling particles are advected farther downstream and help create the stratiform portion of the MCS. Aircraft probes are capable of determining hydrometeors and their microphysical properties, including their bulk water and ice content. In conjunction with airborne radars, these probes have been used to relate the microphysical and kinematic fields

[e.g. *Zrnić et al.,* 1993; *Hogan et al.*, 2002; *Bouniol et al.*, 2010]. However, probe data has limited temporal and areal coverage since it is restricted to the aircraft's flight path. Additionally, while airborne probes are capable of sampling frozen, mixed phase, and liquid hydrometeors, it is nearly impossible to simultaneously sample all three phases for a long period of time. Dual-polarimetric radars have the benefit of being able to identify microphysical and hydrometeor features continuously over broad three-dimensional spaces for long durations.

Previous radar studies have provided insight into the relationship between the kinematic and microphysical structure in midlatitude and tropical land regions. *Evaristo et al.* [2010] approximated the three-dimensional wind field of a West African squall line and compared it to the vertical structure of the hydrometeors identified by the PID. *Höller et al.* [1994] and *Tessendorf et al.* [2005] both used the PID as a tool to understand hail trajectories and growth processes in supercell thunderstorms. However, relatively little is known about these kinematic and microphysical relationships in tropical, oceanic regions. While the kinematic structure of mature MCSs is fundamentally similar throughout the globe [e.g. *Zipser,* 1977; *Keenan and Carbone,* 1992; *LeMone et al.,* 1998], differences in the thermodynamic profile, aerosol content, and convective intensity [e.g. *Zipser and LeMone,* 1980; *LeMone and Zipser*, 1980] cause the hydrometeor structure in tropical, oceanic MCSs to differ from midlatitude and terrestrial MCSs. Additionally, *Houze* [1989] demonstrated that the convective regions of mesoscale systems have different vertical velocity profiles in different tropical oceanic regions. Thus, the hydrometeor structure of MCSs likely differs between different oceanic regions. Relatively few studies have been conducted in the central Indian Ocean. It is important to resolve this knowledge gap and increase our understanding of precipitation processes in mature MCSs associated with the

Madden-Julian Oscillation (MJO) in the central Indian Ocean, so that accurate parameterizations can be developed and the validity of numerical simulations can be more rigorously assessed.

The National Center for Atmospheric Research (NCAR) S-PolKa radar was deployed during the Dynamics of the Madden-Julian Oscillation/Atmospheric Radiation Measurement-MJO Investigation Experiment (DYNAMO/AMIE) in the equatorial Indian Ocean to document the structure and variability of the cloud population associated with the MJO [*Yoneyama et al.*, 2013]. The dual-polarimetric and Doppler capabilities of this radar enable the current study to directly investigate the association between the airflow and hydrometeors within mature tropical, oceanic MCSs.

The dual-polarimetric radar signatures of different hydrometeors are so complex that manual analysis is prohibitively time consuming for large samples of data. In order to aid in the analysis of this complicated data, NCAR has developed a particle identification algorithm (PID) that is applied to dual-polarimetric data to identify the most likely dominant hydrometeor from a given volume of radar data [*Vivekanandan et al*., 1999]. *Rowe and Houze* [2014] composited PID data collected by the S-PolKa radar during DYNAMO/AMIE and investigated how the frequency and vertical profile of hydrometeors varied between three active periods of the MJO. They examined MCSs and smaller storms, which they called sub-MCSs. They concluded that the frequency of different hydrometeor types vary with storm size and MJO active event. However, the mean shape of the vertical profile showed little variation, differing only according to whether they were located in the convective or stratiform portions of the precipitating cloud systems. Given that *Rowe and Houze* [2014] only considered the mesoscale vertical profile of hydrometeor occurrence, the current study expands upon their results by relating these hydrometeors to the dynamical structure of mature MCSs at the convective scale.

The goal of our work is to give insight into the dynamics and microphysics of MJO convection in the central Indian Ocean. In other regions of the world previous studies have investigated the association between the kinematic and hydrometeor structure through case analyses. While these studies provide insight into specific storms, case studies do not indicate if their results are robust features of all storms. The current study is, to our knowledge, the first in which dual-polarimetric radar data is used to composite multiple cases and directly show that different types of hydrometeors are organized in a repeatable and systematic fashion around the dynamical structure of mature tropical oceanic MCSs. Based on our composites we develop conceptual models that directly associate the kinematic and hydrometeor structures of mature, oceanic MCSs in the central Indian Ocean during the active MJO. The systematic relationships demonstrated in these conceptual models are important since the hydrometeor fields derived in this study are indicative of microphysical processes and their relation to storm-scale air motions. Subsequent studies can use these conceptual models to test and develop parameterizations in tropical oceanic cloud systems and validate the interactions of dynamics and microphysics within numerical simulations.

2. Data / Methodology

2.1 S-PolKa data and the Particle Identification Algorithm

The NCAR S-PolKa radar is a dual-wavelength (10.7 and 0.8 cm), dual-polarimetric, Doppler radar that was deployed during DYNAMO/AMIE on Addu Atoll (0.6°S, 73.1°E) in the

Maldives from 1 October 2011 through 14 January 2012. It has a beam with of 0.92° and peak power of 600 kW. The radar's scan strategy, which is detailed in *Zuluaga and Houze* [2013], *Powell and Houze* [2013], and *Rowe and Houze* [2014], included a series of elevation-angle scans at fixed azimuths (referred to in radar terminology as range-height indicator, or RHI, scans) that were horizontally spaced every two degrees between azimuthal angles 4°- 82° and 114°-140°. These RHIs provided vertical cross-sections of the cloud population recorded between elevation angles of 0° and 45°. This study only considers the 10.7 cm (S-band) wavelength RHI scans within 100 km of the radar (black regions in Figure 1). Beyond that range the antenna's 0.92° beam width does not provide sufficient resolution. S-PolKa's post-experiment data processing procedures are detailed in *Powell and Houze* [2013] and *Rowe and Houze* [2014]. Given that Addu Atoll is less than three meters above sea level and isolated from larger land masses, S-PolKa provides one of the first polarimetric datasets of purely tropical, oceanic convection.

This study focuses on the eleven rainy periods identified and analyzed by *Zuluaga and Houze* [2013]. Each of the rain events is a 48-hr period centered on a maximum in the running-mean of the 24-hr total accumulated rain observed by the S-PolKa radar. All of these rain events occurred during active periods of the MJO, when MCSs are most prevalent [e.g. *Chen et al.*, 1996; *Houze et al.*, 2000; *Rowe and Houze*, 2014].

Within the eleven rain events, the current study identifies individual radial velocity RHIs that display layer lifting consistent with the convective updraft and midlevel inflow trajectories shown in Figure 2 from *Kingsmill and Houze* [1999a]. The rearward tilt associated with the convective updraft is a standard feature of mature convective elements that is associated with negative horizontal vorticity generated by the horizontal gradient of buoyancy at the edge of the

downdraft cold pool [*Rotunno et al.,* 1988]. Thus, the convective regions identified in this study are representative of the mature stage of a generic deep convective cell. As will be illustrated below, this structure is so robust that it is easily identified in single-Doppler radar data as a channel of air entering from the boundary layer, tilting upward where it converges with oppositely flowing air associated with the downdraft, and reaching a point at cell top where the flow splits as a result of cloud-top divergence. Mature stratiform regions are characterized by a layer of a subsiding midlevel inflow that has lighter rain and a melting-layer bright band [*Kingsmill and Houze,* 1999a]. Convective updraft and midlevel inflow layers are routinely observed in DYNAMO/AMIE dataset and persist for long periods of time. Isolated or small convection and MCSs that have recently formed may not have these kinematic structures and are thus excluded from this study. Mature MCSs are an important component of the MJO cloud population, especially due to their top heavy latent heating profile [*Barnes et al.*, submitted].

We have selected RHIs based only on their radial velocity structure; they are not selected on the basis of their dual-polarimetric variables. This detail is important since, as will be explained below, we composite the latter relative to the kinematic structure seen in the radial velocity field. In order to avoid biasing our results towards any one storm, only one RHI from an MCS's convective and/or stratiform region is selected. When a storm has multiple RHIs with layer lifting, only the RHI with the most distinct airflow layers is selected. Using this criteria we identify 25 mature convective inflow RHIs and 37 mature stratiform midlevel inflow RHIs. The stratiform RHIs are further subdivided into 9 stratiform RHIs with a leading-convective line and 28 stratiform RHIs without a leading-convective line, for reasons discussed below. The requirement that only one RHI be taken from each convective/stratiform region is one of the largest limitations on the size of our dataset since we commonly observed layer lifting in 5-10

RHIs from each MCS. *Kingsmill and Houze* [1999a] showed that the airflow through a mature MCS is highly three-dimensional with the direction of the lower-level updraft inflow and midlevel downdraft inflow being determined by the direction of the large-scale environmental wind. Therefore, the inflow intensities may be underestimated in our composites and we do not base any results on the intensity of the inflows, only on their slopes.

S-PolKa's alternating horizontally and vertically polarized pulses allows us to calculate several dual-polarimetric radar variables that provide information about the dominant types of hydrometeors affecting MCS precipitation. These variables include differential reflectivity (Z_{DR}), specific differential phase (K_{DP}), correlation coefficient (ρ_{hv}), and linear depolarization ratio (LDR) and they indicate the size, shape, orientation, and water phase of the hydrometeors. Z_{DR} is sensitive to the tumbling motion, shape, density, and dielectric constant of hydrometeors. Large, oblate particles have Z_{DR} values greater than zero. Hydrometeors that are nearly spherical and/or tumbling have Z_{DR} values near zero. Because of the sensitivity of Z_{DR} to the dielectric constant of the target, dry ice particles have lower values of Z_{DR} than liquid water drops or water-coated ice particles of the same size. K_{DP} is also sensitive to the orientation and dielectric constant of the hydrometeors, which results in large, oblate raindrops being characterized by very high K_{DP} values and ice particle aggregates having slightly elevated values. ρ_{hv} indicates the diversity in the size, shape, orientation, and water phase of the hydrometeor population. Most meteorological echoes are associated with a ρ_{hv} of nearly one but ρ_{hv} decreases to between 0.95-0.85 when the hydrometeor population becomes more diverse. LDR also indicates the hydrometeor diversity within a radar sample volume. While large negative values of LDR indicate that the hydrometeor population is uniform, small negative LDR values indicate that the hydrometeors within the radar echo volume are tumbling, oriented, and/or have different sizes, shapes, and water phases. For a

comprehensive description of dual-polarimetric radar variables see *Bringi and Chandrasekar* [2001].

Vivekanandan et al. [1999] developed a particle identification algorithm (PID) that uses these dual-polarimetric variables and the closest rawinsonde temperature profile in a fuzzy logic algorithm to identify the type of hydrometeor that dominates the radar reflection from a given a volume of the atmosphere (referred to as the radar sample volume). The sounding data used in this study to determine the temperature profile were obtained from a rawinsonde station approximately 10 km from the radar site and were part of the DYNAMO/AMIE sounding array described by *Ciesielski et al.* [2014]. Each hydrometeor type classified by the PID is independently assigned an interest value between 0 and 1, which represents the likelihood of that hydrometeor being the dominant particle in that radar sample volume. The interest value is based on the weighted sum of two-dimensional membership functions, which express the dual-polarimetric and temperature ranges associated with each type of hydrometeor. Table 1 provides the approximate dual-polarimetric and temperatures ranges specified by the membership functions during DYNAMO/AMIE. The hydrometeor type with the largest interest value (i.e. closest to one) is output by the PID. The hydrometeor types analyzed in this study include: heavy rain (HR), moderate rain (MR), light rain (LR), graupel/rimed aggregates (G/RA), wet aggregates (WA), dry aggregates (DA), small ice particles (SI), and horizontally-oriented ice crystals (HI). The physical meaning of these categories will be discussed below.

While the PID is an extremely powerful tool, the algorithm has limitations. First, the PID only identifies the dominant hydrometeor type. The PID algorithm does not describe every type of particle present in the radar sample volume and the dominant hydrometeor type is not necessarily the most prevalent particle. Rather, the algorithm tends to describe the particle that is

the largest, densest, and/or has the highest dielectric constant. For example, a few large aggregates will produce a return radar signal that is much stronger than the return from small ice crystals, even if the ice crystals are far more prevalent. This problem becomes more serious with distance from the radar since the size of the radar sample volume increases with range [*Park et al.,* 2009]. The impact of this limitation is explored in greater detail below. The accuracy of the PID is also limited since the theoretical associations between polarimetric variables and hydrometeor types are complex and the polarimetric boundaries of different hydrometeor types often overlap [*Straka et al.,* 1999]. However, as *Vivekanadan et al.* [1999] point out, the soft boundaries in the PID allow for the fuzzy logic method to be one of the best methods to handle these complex relationships. Unfortunately, it is difficult to validate the complex relationships employed by the PID with aircraft data since it only identifies the dominant hydrometeor type. A few of the studies that conduct such a comparison are discussed below. The validity of the PID is also impacted by the quality of the radar data, which is degraded by non-uniform beam filling, attenuation, partial beam blockage, and noise. While studies such as *Park et al.* [2009] explicitly account for these factors in their PID algorithm, this study does not. However, we do not think that these radar quality issues are serious problems in our data. The S-PolKa radar experienced very little attenuation during DYNAMO/AMIE. Beam blockage is not an issue since both RHI sectors have an unobstructed view of the ocean. S-PolKa data becomes noisy near the edges of the echo, but this only has a minor effect on our results since we manually removed these areas. Finally, the PID is limited by the accuracy of the assumed temperature profile. For example, errors in the height of the melting level can incorrectly place rain about wet aggregates. We have manually edited the temperature profiles to try to mitigate this problem.

2.2 Graupel and rimed aggregates

The process of an ice crystal collecting supercooled water droplets is called riming. Graupel is a hydrometeor that has undergone so much riming that the ice particle's original crystalline structure is no longer distinguishable. While dual-polarimetric data allow us to identify when riming has occurred, they do not provide a measure of the degree of riming and we cannot know with certainty that a particle is sufficiently rimed to be characterized as graupel. Thus, the dual-polarimetric radar returns from a graupel particle are difficult to distinguish from those of a large aggregate of ice particles that has been affected by some riming but not enough to disguise its composition as an aggregate of ice crystals. To indicate this uncertainty, the PID includes a category called "graupel/rimed aggregates (G/RA)." This uncertainty in G/RA distinction is not an especially serious handicap since our primary goal is to determine where riming is likely to have been occurring.

2.3 Distinctiveness of the hydrometeor categories and validation by aircraft

Due to the limitations of the PID algorithm it is important to investigate the validity of the DYNAMO/AMIE PID. The Centre National d'Etudes Spatiales (CNES) Falcon aircraft was stationed on Addu Atoll from 22 November through 8 December 2011 [*Yoneyama et al.,* 2013]. Based on a few flights tracks within the S-PolKa domain, *Martini and Viltard* [2014] concluded that the PID classifications were generally accurate. However, since *Martini and Viltard's* [2014] study was restricted to a small dataset, we analyzed the PID's accuracy through several more

comprehensive methods. As stated above, membership functions are used in the PID to define the range of polarimetric values and temperatures associated with each hydrometeor type. Table 1 shows that these membership functions often overlap. Thus, before using the PID we must establish that each of the eight hydrometeor types isolate radar sample volumes that have unique dominant hydrometeor species. Figure 3 shows the observed distribution of polarimetric variables of all radar sample volumes classified as a given hydrometeor type within the mature convective and stratiform regions we analyze. The red line is the median of those radar sample volumes, the blue lines are the 25% and 75% quartiles, the black lines encompass 99.3% of the data, and the red stars are outliers. Based on Figure 3 it is evident that the fuzzy logic method classifies the dominant hydrometeors into groups with unique observed polarimetric properties.

2.4 Examples of the PID algorithm choices and associated uncertainty

As mentioned previously, the PID assigns each hydrometeor type an interest value between 0 and 1 to indicate the likelihood of that particle type being the dominant hydrometeor in that radar sample volume. The difference between the two largest interest values can be interpreted as a measure of certainty in the classification. Larger differences indicate that the polarimetric data is consistent with the presence of only one dominant type of hydrometeor. Small differences indicate that the polarimetric data is being influenced by multiple hydrometeor types. Figure 4 illustrates the use of the interest value difference as a way of gauging certainty in the PID's choice of dominant hydrometeor type for a convective updraft and a stratiform midlevel inflow example. Figures 4a and d show the hydrometeor type with the largest interest value (1st PID), Figures 4b and e show the hydrometeor type with the second largest interest value (2nd PID), and

the difference between the interest values of the 1st and 2nd PID is shown in Figures 4c and f. In order for the algorithm to classify a hydrometeor type it must have an interest value of at least 0.5. White regions in the 2nd PID (Figure 4b and e) near 5 km and in the upper portions of the stratiform midlevel inflow region represent regions where only one hydrometeor type satisfies the 0.5 requirement.

Near the 5 km level, red colors in Figures 4c and f indicate large interest value differences and very high certainty that a single type of particle dominates the radar echo. In both the convective and stratiform cases, the radar echo in this layer is overwhelmingly dominated by WA; Figures 4b and e shows that no second particle type is identified. This structure marks the melting layer and is consistent with these regions containing a mixture of frozen particles that are falling and melting. In the convective example, high certainty is also seen as narrow spikes of large interest value differences that occur above the 5 km and extend up to 10 km. These spikes suggest that the algorithm is certain that at least a small region of DA surrounds the G/RA particles in convective elements. However, the reduced interest value differences surrounding these spikes indicate that the full spatial extent occupied by DA is less certain.

While Figure 3 indicates that the hydrometeor types are statistically associated with distinct polarimetric characteristics, it is important that we analyze the spatial distribution of the particles since the overlapping membership functions could cause the classification in regions of small interest value differences to be somewhat random from one point to the next. This randomness does not appear to be a problem, all hydrometeors appear to be organized in a physically meaningful manner. The blue colors in Figures 4c and f indicate that both the convective and stratiform examples have a region of reduced PID certainty above 5 km (the approximate 0°C level) with DA as the 1st PID and SI as the 2nd PID. This result is reasonable in glaciated regions

because ice hydrometeors are of a similar character but have a continuous spectrum of sizes. The DA category corresponds to larger ice particles, while the SI category corresponds to smaller ice particles. The final judgment of the PID algorithm (Figure 4a) in the convective example indicates that the larger DA are the dominant producer of the radar signal, which is physically reasonable since the turbulent air motions within the upper portion of the cell cause ice particles to clump into large aggregates and these large particles are more readily detected by the radar. However, the small interest value differences throughout this region (Figure 4c) suggests that smaller SI particles are also likely present and it is difficult to say which particle type is most numerous at a given point in time and space. Around the edges of the echo the PID expresses certainty that the SI particles dominate. This gradation from interior core to outer edge of the upper echo is another physically reasonable result of the PID in the convective echo.

The certainty associated with the frozen hydrometeors also accurately represents the inherent variability of the hydrometeor population. Between 5 and 8 km, the PID's first choice is the larger DA (Figure 4d) and its strong second choice is SI (Figure 4e and f). In the first few kilometers above the melting layer branched crystals and larger aggregates are expected [*Houze and Churchill* 1987; *Houze* 2014, p. 58-59] and their large size causes them to dominate the radar signal. Therefore, it is reasonable that the PID detects larger particles in this layer even though the 2nd PID suggests that many smaller ice particles are also likely present. In the uppermost kilometers of the stratiform echo, Figure 4d and e reveals that the PID algorithm is highly certain that SI are the dominant particle type, there is no viable second hydrometeor type. This zone corresponds to the red region in Figure 4f, which is a quantitative indication of this very high certainty. Given that vertical motions in the stratiform regions are relatively weak and cannot generate large aggregates or advect them upward, it is physically reasonable that the PID

identifies only SI in the upper portions. Thus, in the glaciated regions of convective and stratiform precipitation, the 1st PID systematically describes the hydrometeor type that dominates radar signal and the 2nd PID portrays the variability of the ice hydrometeor population.

The PID algorithm is less certain in its G/RA category. These particles are seen in the convective case as four spikes extending up to 8 km in height and in the stratiform case as shallow, intermittent pockets along the top of the WA layer (Figure 4a and d). In both examples, these G/RA regions are characterized by small interest value differences (Figures 4c and f) and their second particle choice is most often the "graupel/rain (G/R)" category (Figure 4b and e, Table 1). The main distinction between the G/RA and G/R categories is that the later suggests that rimed particles are melting and mixed with liquid hydrometeors. Combining the 1st and 2nd PID suggests that rimed particles are present and may be starting to melt, which is physically reasonable since the regions of G/R in the 2nd PID are very near the melting level at 5 km. While G/RA are expected in the convective example, the presence of G/RA in stratiform regions might seem surprising. However, we will show that such occurrences have been observed in previous studies and is physically reasonable.

The reduced certainty is not always an indication of the natural variability in the hydrometeor population. Evaluation of the 2nd PID on a case by case basis is important. Figures 4c and f show a region of small interest value differences below the melting layer at ~3-4 km altitude, which is at the top of the rain layer in both the convective and stratiform cases. This uncertainty in the PID output occurs because the 2nd PID algorithm is incorrectly identifying large raindrops as WA, as indicated by Figures 4b and e. At this level, the temperature in the Gan soundings (not shown) are too warm for WA to exist. Therefore, we are confident that only the rain categories

shown in the 1st PID are correct. Since we only use the 1st PID in our composites, this misclassification in the 2nd PID does not impact our results.

While the PID does not comprehensively describe every type of particle present in a radar sample volume, the comparison of the PID's first and second choices gives us a high level of confidence that the algorithm's first choice provides a physically reasonable assessment of the dominate hydrometeor type. Our confidence in the PID is further bolstered since even the 2nd PID is physically reasonable above the melting level and consistent with the known variability of the hydrometeor population. We find similar patterns in the 1st and 2nd PID fields in the other convective and stratiform RHIs considered in this study.

In order to investigate the sensitivity of our results to the NCAR PID methodology, we ran a different fuzzy logic based hydrometeor classification algorithm, described by *Dolan and Rutledge* [2009] and *Dolan et al.* [2013]. Figures 6 and 7 in *Rowe and Houze* [2014] indicate that the two algorithms produce similar hydrometeor structures and supports the presence of DA and G/RA above the melting layer.

2.5 Compositing Technique

Spatial compositing of RHIs allows this study to directly determine where hydrometeors occur in relation to the air motion patterns in the convective and stratiform portions of mature oceanic, tropical MCSs and assess the consistency of those relationships. Although, mature convective and stratiform regions exhibit systematic airflow patterns, these patterns do not always occur on the same horizontal scale. The relationship between the hydrometeors and

airflow is most clear when each individual convective and stratiform RHI is scaled to a common size. Our compositing method consists of four-steps. To illustrate these steps, we consider a convective updraft layer with a contiguous region of WA identified by the PID algorithm.

1. Identify the portion of the radial velocity RHI that contains the convective updraft layer. This "convective updraft region" is determined according to the radial-velocity convergence and divergence signatures. In the horizontal direction, the region is bounded by the convergence near the surface and the width of the divergence signature aloft. The vertical extent of the convective region starts at the surface and ends where the echo becomes too weak to be detectable (typically at approximately the 5 dBZ echo contour). Figure 5e shows an example of a convective updraft region identified in this way. The solid black lines surround the convective element. Table 2 lists the width and height of each convective region so identified. The width of our convective updrafts (Table 2) are roughly comparable to the width observed during TOGA COARE by *Kingsmill and Houze* [1999a] (Figure 2a).
2. Draw a line to approximate the center of the sloping convective updraft (dashed black line in Figure 5e). This line starts at the surface, where the convergent updraft layer begins to slope upward, and ends at the center of the base of the radial-velocity divergence signature. Table 2 lists the slopes of all updrafts so identified. The slope of our convective updrafts (Table 2) are comparable to the width observed during TOGA COARE by *Kingsmill and Houze* [1999a] (Figure 2a).
3. Draw a polygon around the contiguous WA region in the PID data. The polygon is drawn manually in order to remove any noise or artifacts in the PID data and is only done if the WA are contiguous over at least two radar sample volumes. Multiple

polygons are outlined if several distinct areas of contiguous WA exist within the convective updraft region.

4. Translate and scale the location of the WA polygon to a generic convective updraft. All convective updrafts do not slope toward the right as shown in Figure 2a. If a convective updraft line slopes towards the left, we first take the mirror image of the convective updraft line and wet aggregate region. This ensures that all convective updraft lines slope towards the right. Then, the convective updraft line is stretched or compressed so that its slope exactly matches the slope of the generic convective updraft. The slope of the generic convective updraft is approximately equal to the mean updraft slope of the 25 convective RHIs. The line is also horizontally translated so that it lies exactly on top of the generic convective updraft. This process provides horizontal and vertical scaling and translation factors, which are then applied to the WA polygon to obtain its location within the generic convective updraft. This scaling process accounts for differences in the slope and horizontal extent of each convective RHI, which is important since Table 2 indicates that the width and slope of our convective updrafts varies substantially.

The four steps outlined above are repeated for all contiguous WA regions in all of our convective updraft RHIs, which results in a composite showing where WA are located relative to the convective updraft as shown in Figure 7c. The sloping black line represents the generic convective updraft and the shading represents the frequency with which WA occur at a given location relative to the updraft. This process is repeated for each of the eight hydrometeor categories analyzed in this study. Since our composites only consider the location of each hydrometeor type relative to the airflow and only contain one RHI scan from each identified

convective updraft region, they do not indicate the overall horizontal coverage-or duration (i.e. the total amount) of the hydrometeors. Our composites are used solely to explore where different types of hydrometeors are located relative to the kinematic structure of a MCS.

Stratiform midlevel inflow regions are subjected to the same compositing technique. The horizontal extent of the stratiform region is based on where the speed of the midlevel inflow exceeds the ambient radial velocity. The midlevel inflow is represented as a line that runs along the base of the accelerated flow. This line starts where the flow begins to converge and accelerate beneath the anvil and terminates where the flow returns near to its ambient speed within the stratiform precipitating region. Figure 6e shows the radial velocity field associated with a stratiform region on 18 November 2011. The solid black lines outline the stratiform midlevel inflow region. The dashed black line shows the midlevel inflow line. Table 3 lists the width and height of each stratiform region and the slope of each midlevel inflow line. The width of our midlevel inflow regions (Table 3) are comparable to the width observed during TOGA COARE by *Kingsmill and Houze* [1999a] (Figure 1b).

3. Hydrometeors in Mature Sloping Convective Updraft Channel

The radial velocity shown in Figure 5e demonstrates that, despite only having radial velocity data, the mature convective updraft is readily apparent. Analyzing the polarimetric data allows us to understand the microphysical processes associated with each hydrometeor type. This case was selected since its polarimetric features are very distinct and are representative of the other convective updraft RHIs. The reflectivity field (Figure 5a) shows four spikes in the 40-dB$_Z$

reflectivity above an altitude of 5 km at widths of 10-20 km. These reflectivity peaks are collocated with low Z_{DR} values (Figure 5c), which suggests that these particles are rimed [e.g. *Aydin and Seliga,* 1984; *Straka et al.,* 2000] and is consistent with the PID's classification of G/RA (Table 1). The moderate reflectivity and low Z_{DR} adjacent to these reflectivity spikes is indicative of aggregated ice crystals [e.g. *Bader et al.,* 1987; *Straka et al.,* 2000; *Andrić et al.*, 2013] and is classified by the PID as DA. These DA are distinct from the melting particles classified as WA since WA have lower ρ_{hv} and higher LDR (Figures 5g-h) [e.g. *Zrnić et al.,* 1993; *Straka et al.*, 2000; *Brandes and Ikeda*, 2004]. Figure 5c shows that Z_{DR} rapidly increases as particles fall below the melting layer. This polarimetric signature can be interpreted as an indication of very large drops and/or heavily water-coated aggregates, which is consistent with HR and is expected given the G/RA above. The high K_{DP} below an altitude of 5 km in Figure 5d further supports the presence of HR below the melting level [e.g. *Straka et al.*, 2000]. Thus, the microphysical and polarimetric characteristics associated with each hydrometeor type are physically reasonable and consistent with previous studies.

Figure 7 shows the hydrometeor composites based on the 25 mature convective updraft RHIs obtained during the active stage of the MJO in the central Indian Ocean. The black line sloping upwards toward the right represents the convective updraft, with flow approaching from the left, ascending in a sloping channel, and diverging at the top. The colors represent the hydrometeors' frequency of occurrence. The color bar varies in each panel so the distribution of each hydrometer type is clearly depicted. The horizontal and vertical axes are expressed as fractions of the width and height of the convective updraft core and are referred to as the normalized width and height, respectively. Given that our spatial compositing technique distorts the vertical axis by stretching and compressing each RHI, the relationship between each frozen hydrometeor type

and temperature is presented in Table 4. Using all radar sample volumes classified as a given hydrometeor table, Table 4 lists the median temperature of each frozen hydrometeor type. Additionally, Table 4 lists the average temperature of the coldest and warmest 10% of each hydrometeor type.

The lack of spatial spread in these composites demonstrates that hydrometeors are organized in a systematic manner with respect to the convective updraft. Below the melting layer, the updraft core is characterized by moderate rain (Figure 7e), which is consistent with previous observations of monsoonal squall lines in the South China Sea [*Jung et al.*, 2012; *Wang and Carey*; 2005] and West African squall lines [*Evaristo et al.*, 2010]. The heaviest rain occurs just downwind of the convective core (Figure 7a), which is expected since the relatively large, heavy drops can only be advected short distances. While these regions of HR are likely co-located with convective-scale downdrafts, which is consistent with the sloping structure of the convective cells, we cannot resolve this downward air motion with single-Doppler radar.

WA sometimes occur at the melting level, and they are slightly more common downwind of the updraft core (Figure 7c). In convective regions, WA are likely associated with small-scale weak upward or downward motion (unsolved by this dataset). Thus, given the vigorous upward motion characteristic of a convective updraft core, it is not surprising that the WA are somewhat less common within the core. WA usually occur in narrow layers but Figure 7c seems to suggest that WA extended over a rather deep layer. A few factors are likely influencing the depth of the WA layer in our composites. Table 2 indicates that the height of the convective cores vary by more than 5 km. Thus, our compositing technique, which scales each core to the same height, distorts the vertical extent of the WA. Additionally, the median temperature of WA is reasonable at -0.98°C (Table 4) but temperatures associated with WA range from -4.9°C to 1.1°C (Table 4),

which is larger than expected. This relatively wide range of cold minimum temperatures could be related to beam broadening since some of the convective RHIs occur nearly 100 km away from the radar. Thus, while we are confident that our composites correctly indicate that WA are more common downwind of the updraft, the vertical extend of these particles are likely less than indicated by our composites. These factors likely influence all of our hydrometeor composites but is most apparent in the WA composite due to the shallow depth of the WA layer.

G/RA occur just behind and below the convective updraft, where we would expect heavier particles to be falling (Figure 7f). *Jung et al.* [2012] suggest that the rapid fall speed of G/RA creates downdrafts beneath the convective updraft. However, these downdrafts cannot be resolved by our dataset. Table 4 indicates that the median temperature of G/RA is -3.7°C and the coldest 10% of G/RA are only -12.7°C on average, which suggests that the vertical extent of these G/RA signatures are often limited to a few kilometers above the melting level and is consistent with *Rowe and Houze* [2014]. DA are the most prevalent hydrometeor above the melting level and dominate the convective updraft (Figure 7g), which is similar to monsoonal squall lines in the South China Sea [*Jung et al.,* 2012].

A relatively thin layer of SI dominate the edges of the convective region (Figure 7d). Note that our analysis of the 2nd PID, which is discussed above, suggests that SI are prevalent through the depth of convective clouds but only dominate the radar signal along the edges of the echo. Pockets of HI frequently are located near echo top; however, this signal might not be meaningful since Z_{DR} and LDR often are noisy in these regions.

4. Conceptual model of hydrometeor occurrence relative to convective region airflow

Based on the systematic and physically reasonable patterns of hydrometeor occurrence discussed above, we have developed a conceptual model for the spatial pattern of hydrometeors within the mature convective updraft regions of MCSs observed during the active stage of the MJO during DYNAMO/AMIE (Figure 8). The black lines represent the convective updraft described in *Kingsmill and Houze* [1999a] and the colors correspond to the different hydrometeor types. Not every hydrometeor type is present in every mature convective updraft. This conceptual diagram shows where a hydrometeor type is most likely to be located relative to the mature convective updraft morphology, if that hydrometeor type is present. Additionally, the hydrometeors depicted in this conceptual model only describe the particles that dominate the radar signal. Hydrometeors that are smaller, less dense, or have a lower dielectric constant are likely present but are not represented.

The coverage of each hydrometeor type is calculated by taking the number of radar sample volumes classified as a given hydrometeor type and dividing it by the total number of sample volumes, regardless of its hydrometeor type. Each radar sample volume is 150 m wide. This coverage describes the hydrometeors' extent in height and one horizontal dimension along the direction of the beam. This spatial coverage is averaged over all convective regions and is listed in the color bar labels. While the denominator in our coverage includes every radar sample volume in the convective updraft region, our manual analysis does not include every sample owing to smoothing and artifact removal. Thus, our coverage percentages do not add to 100%. DA account for over 20% of the radar sample volumes and are the most prevalent particles in the convective region. MR covers slightly more area than HR or LR. G/RA have the smallest areal

coverage at 2%. Since we only analyze one RHI from each storm, we cannot determine the overall volumetric coverage of the hydrometeors in the storm.

The first column in Table 5 shows the percentage of our mature convective updraft RHIs that contain at least one contiguous region of a given hydrometeor type. MR and DA were present in all 25 convective updraft regions. G/RA occurred 88% of the time. We emphasize, however, that since we only select RHIs that contained a clear, distinct convective updraft, these percentages specifically refer to convection that is either in its mature stage or just beginning to weaken, i.e. when particles classified as G/RA would most likely occur. Since we are only considering the location of these hydrometeors in single RHIs we cannot comment how their frequency varies during the lifecycle of a convective updraft. These matters will need to be resolved by modeling, which is beyond the scope of this study.

5. Hydrometeors in Mature Stratiform Midlevel Inflow Layer

Figure 6e shows the increased radial velocity associated with the descending midlevel inflow at an altitude of 3-5 km. While other RHIs display stronger midlevel inflow layers, this example was chosen since the localized radial velocity acceleration associated with the midlevel inflow is readily apparent between widths of 10-45 km and clearly demonstrates how the stratiform region is defined. Once again, we start by analyzing the polarimetric fields associated with one RHI to demonstrate which microphysical processes are associated with each hydrometeor type. The top of the stratiform region is characterized by low reflectivity and slightly elevated values of Z_{DR} (Figures 6a and c), which is consistent with ice crystals and the PID's SI category (Table 1). As

the stratiform inflow descends through the layer between 5 and 10 km, reflectivity increases but Z_{DR} decreases (Figures 6a and c) which is often associated with aggregation [e.g. *Bader et al.*,1987; *Straka et al.,* 2000; *Andrić et al.,* 2013] and is consistent with the PID's classification of DA. The general transition from SI to DA likely results from the relatively quiescent structure of the stratiform region, which allows ice particles to gradually settle as they slowly take on mass via vapor deposition and produce much larger particles through aggregation with each other [*Houze,* 1997; *Bechini et al.,* 2013]. However, while DA dominate the radar signal at altitudes between 5-10 km due to their large size, these DA are not the only frozen hydrometeors present in this layer. Our analysis of the 2nd PID, which is discussed above, suggests that SI are likely numerous above the melting level but only dominate the radar signal at high altitudes. As aggregates fall through the melting zone between 4-5 km they develop a layer of water on their exterior and begin to melt at different rates, which causes an increase in reflectivity, Z_{DR}, and LDR and a decrease in ρ_{hv} (Figure 6a,c,g-h) [e.g. *Zrnić et al.,* 1993; *Straka et al.,* 2000; *Brandes and Ikeda*, 2004]. All particles in the melting layer are characterized as WA (Table 1).

The polarimetric data contain several localized features that provide details about unique microphysical processes that occur within turbulent portions of the stratiform region. Figures 6a, c, g, and h, show that low reflectivity, high Z_{DR}, low ρ_{hv}, and high LDR occur between altitudes of ~8-10 km and widths of 35-40 km. Low reflectivity indicates that these particles are relatively small and Z_{DR} values of 1-2 dB indicate that these particles are horizontally oriented. While the hydrometeors are preferentially oriented in a horizontal direction, the low ρ_{hv} and low LDR indicates that the tilt of each hydrometeor varies slightly. According to Table 1, these particles are identified as HI. To understand the microphysical processes responsible for these hydrometeors consider the radial velocity and temperature fields (Figures 6e-f). Note that these

crystals occur in a region where outbound and inbound radial velocities are in close proximity and temperatures are between -10°C and -20°C. The vertical wind shear likely produces turbulence and hence isolated regions of super-saturation that, in this temperature range, facilitate enhanced depositional growth of large dendritic crystals [*Mason,* 1971; *Hobbs*, 1974]. This conclusion is consistent with analyses presented in *Houze and Churchill* [1987], *Wolde and Vali* [2001], *Hogan et al.* [2002], *Andrić et al.*, [2013], and *Bechini et al.,* [2013]. Note that reflectivity increases, ZDR decreases, and ρ_{hv} increases immediately below this dendritic growth region, which indicates that these dendrites rapidly aggregate and is consistent with DA immediately below the HI.

Another interesting, though isolated, microphysical feature indicated by the PID is the occurrence of discrete pockets of particles classified as G/RA along the top of the WA layer in Figure 6b. *Rowe and Houze* [2014] also found this feature in their vertical PID profiles within stratiform regions. Figure 9 shows two sets of vertical profiles of reflectivity and Z_{DR} through a portion of the RHI shown in Figure 6. One set of vertical profiles contains G/RA above the WA layer. The other set only contains WA. The colored dots show where each hydrometeor type is located with respect to the polarimetric profiles with G/RA in green and WA in dark blue. While both reflectivity profiles have a bright band whose intensity is greater than 40 dBZ, Figures 9b and d show that G/RA are identified when Z_{DR} is low and WA are identified when relatively high Z_{DR} exists. Thus, low Z_{DR} discriminates G/RA from WA. This pattern of high reflectivity and low Z_{DR} is indicative of riming [e.g. *Aydin and Seliga,* 1984; *Straka et al.,* 2000].

The occurrence of riming within the stratiform region of MCSs is supported with in situ observations. In the central Indian Ocean, *Suzuki et al.* [2006] reported pictures indicative of rimed particles within stratiform regions from videosondes used during the Mirai Indian Ocean

Cruise for the Study of the MJO-Convection Onset (MISMO) in 2005. *Martini and Viltard* [2014] found quasi-spherical, rimed particles within stratiform regions observed by the CNES Falcon aircraft during DYNAMO/AMIE. Additionally, precipitation image probe data from the NOAA P-3 found graupel during DYNAMO/AMIE as it descended through the melting level of a MCS to the east of the S-PolKa domain on 24 November 2011 [*N. Guy*, personal communication, 2014]. The presence of rimed particles near the melting level in stratiform regions is not unique to the central Indian Ocean. Using data from GATE and deductive reasoning *Leary and Houze* [1979b] foresaw that rimed particles were likely located atop the melting layer. Evidence of the likelihood of rimed hydrometeors within stratiform regions has also been found in numerical simulations and observational studies in the equatorial maritime continent [*Takahashi and Kuhara*, 1992; *Takahashi et al.,* 1995], West Africa [*Evaristo et al.,* 2010; *Bouniol et al.*, 2010], Oklahoma [*Zrnić et al.,* 1993], Taiwan [*Jung et al,* 2012], and Europe [*Hogan et al.,* 2002].

While these rimed aggregates may be left over from collapsing deep convection [*Zrnić et al.,* 1993; *Leary and Houze,* 1979b], small-scale convection embedded within the mesoscale updraft could produce enough supercooled water for graupel to develop within the stratiform region itself [*Hogan et al.*, 2002; *Houze and Medina,* 2005; *Houser and Bluestein*, 2011]. The majority of the hydrometeors in the stratiform region gradually descend since their terminal velocity is greater than the mesoscale updraft. However, vertical wind shear along the boundary between the midlevel inflow and mesoscale updraft can be strong enough for Kelvin-Helmholtz instability to develop and create localized regions of upward motion capable of generating supercooled water [*Hogan et al.,* 2002; *Houser and Bluestein*, 2011]. It is unclear which of these mechanism is responsible for the G/RA observed in Figure 6 from 0150 UTC 18 November 2011. Deep

convection associated with the stratiform region completely collapsed by 0100 UTC 18 November but a loop of the PID (not shown) indicates that G/RA appeared near the brightband shortly after 0030 UTC, expanded, and persisted till 0215 UTC. Kelvin-Helmholtz Instability is associated with a bulk Richardson number less than 0.25 in a stably stratified environment [*Miles and Howard,* 1964]. The nearest sounding occurred at 0300 UTC and the bulk Richardson number evaluated between 3 and 6 km, which experienced the largest change in wind direction, was 0.25. Thus, these G/RA could come from the deep convection that collapsed by 0100 UTC, Kelvin-Helmholtz instability, or a combination of the two.

6. Stratiform regions with and without leading-line structure

Stratiform midlevel inflow layers occurred within mature MCSs with two fundamentally different structural morphologies during DYNAMO/AMIE. One type of stratiform region seen frequently by S-PolKa had a very complex structure, in which convective cells entered, intensified, and collapsed within the stratiform region in the manner described by *Yamada et al*. [2010]. We refer to these storms as stratiform without a leading-convective line and Figure 6 is an example taken from one such storm. However, a fundamentally different storm morphology was witnessed in late November and late December 2011 when stratiform regions were proceeded by a convective line and both rapidly propagated rapidly towards the east as one unit. These storms are referred to as leading-line/trailing-stratiform MCSs. *Rowe and Houze* [2014] found that WA occurred less frequently when the stratiform region was behind a leading-convective line. Because of these different mesoscale morphologies, and the hydrometeor differences discussed by *Rowe and Houze* [2014], we construct separate hydrometeor composites

for mature stratiform regions with and without a leading-convective line. Table 3 indicates which RHIs are associated with a leading-convective line.

The composite results of the 28 RHIs of stratiform echoes without a leading convective line are shown in Figure 10. The black line represents the midlevel inflow geometry with the air entering beneath the anvil on the right side of each panel and descending toward the center of the storm on the left side of each panel. The horizontal and vertical axes are expressed as fractions of the width of the midlevel inflow and the height of its base. These fractions are referred to as the normalized width and height, respectively. Hydrometeors are systematically organized around the midlevel inflow. Below the melting level, the rain intensity systematically decreases toward the anvil (toward the right), as expected since the stratiform updraft gradually ascends toward the rear of the storm (Figure 10a, e, and b). Similar to *Evaristo et al.* [2010] most of the rain is light. HR is rare, but tends to occur if the midlevel inflow reaches the surface, which suggests that such stratiform RHIs are slightly more convective. Above the melting layer, the hydrometeors are layered, with WA at the melting level and bands of DA and SI at sequentially higher levels (Figure 10c, g, and d). The layered structure is also apparent in Table 4, which shows a systematic decrease in the median temperature of WA, G/RA, DA, SI, and HI for mature stratiform without a leading line. The stratiform region of continental MCSs [*Park et al.,* 2009; *Bechini et al.,* 2013] and squall lines in Taiwan [*Jung et al.,* 2012] and in the West Pacific [*Churchill and Houze,* 1987; *Evaristo et al.,* 2010] also have a similar layered structure. The composites also capture the small-scale G/RA and HI features (Figure 10f and h) discussed above. The median temperature of HI is -17.6°C (Table 4), which is within the -10°C to -20°C temperature range that favors the dendritic growth by vapor depositions [e.g. *Bechini et al.* 2013]. However, the average coldest HI temperatures are well below -20°C since there are a few

RHIs that have HI along its echo top. However, similar to instances of HI in the convective updraft RHIs, we are less confident in these echo top signatures due to increased noise.

While the composites of the mature stratiform regions with a leading-convective line only contains 9 RHIs (not shown), and are be too small to allow for statistical conclusions, they are qualitatively similar to the mature stratiform regions without a leading-convective line composites. Additionally, the two types of mature stratiform regions have similar temperatures (Table 4) and hydrometeor frequencies (Table 5). There are several reasons why we might expect these basically similar structures. First, despite their morphological differences both types of stratiform are characterized by an ascending mesoscale flow at upper levels, which will result in the rain intensity systematically decreasing toward the anvil. Second, because the stratiform regions are relatively quiescent in both cases, most ice particles gravitationally settle while growing by deposition and aggregation, leaving the stratiform region with its layered structure of smaller particles at higher levels and larger particles below [*Houze*, 1997; *Bechini et al.*, 2013].The similarity of the hydrometeor structure in stratiform regions with and without a leading-line emphasizes that the kinematic structure of a mature MCS is a strong organization mechanism for hydrometeors.

7. Conceptual model of hydrometeor occurrence relative to stratiform region airflow

Figure 11 presents a conceptual model for the organization of hydrometeors with respect to the midlevel inflow of mature stratiform regions in MCSs. The black lines in Figure 11 show the kinematic structure of the mature stratiform midlevel inflow layer identified by *Kingsmill and*

Houze [1999a]. As in Figure 8, the colored regions in Figure 11 represent the location of the dominant hydrometeor and the percentages in the color bar describe the average coverage of each hydrometeor type in our mature midlevel inflow RHIs. Not every stratiform region contains every hydrometeor type. Thus, Figure 11 shows where a hydrometeor type is most likely to occur relative to the midlevel inflow, if that hydrometeor type is present. Additionally, hydrometeors that are smaller, less dense, or have a lower dielectric constant are likely present but not represented. LR dominates below the melting level with an average coverage of 30%. Above the melting level, SI (20% coverage) are slightly more prevalent than DA (16% coverage). HI and G/RA represent a small portion of the overall hydrometeor coverage in stratiform regions due to the fact that they occur in isolated, thin layers. WA are an important signature of the melting layer and are especially prominent in the most intense stratiform regions. Since we are only considering the location of these hydrometeors in single RHIs we cannot comment on the volumetric concentration of these hydrometeors or how the hydrometeors and their frequencies vary during the lifecycle of a stratiform region.

Table 5 shows the percentage of stratiform RHIs that contain at least one contiguous region of a given hydrometeor type. The differences between the two types of stratiform regions are very small, which supports only having one conceptual model for the stratiform portion of an MCS. LR, WA, and DA are always present and HR is rarely observed. Our dataset contains G/RA in approximately two-thirds of the mature stratiform RHIs. However, we examine RHIs wherein the midlevel inflow is especially distinct and are more likely to have strong instability along the boundary between the descending midlevel inflow and stratiform updraft, which is precisely the situations which favor riming [*Zrnić et al.,* 1993; *Leary and Houze*, 1999a; *Hogan et al.,* 2002]. *Rowe and Houze* [2014] considered all RHIs within the stratiform region and found

that pockets of G/RA pockets occurred relatively infrequently in the overall sense. It thus appears that the well-defined midlevel inflow structure favors the occurrence of the pockets of G/RA. A similar consideration may also account for the relatively high frequency of HI (i.e. dendritic growth).

8. Conclusions

The S-PolKa radar was deployed as part of the DYNAMO/AMIE field campaign on Addu Atoll in the Maldives with dual-polarimetric and Doppler capabilities. *Moncrieff* [1992] and *Kingsmill and Houze* [1999a] used numerical simulations and airborne radar data, respectively, to demonstrate that air moves through mature MCSs in distinct layers. S-PolKa's Doppler capability allows us to identify the convective updraft and stratiform midlevel inflow layers that are discussed in those papers. Additionally, since S-PolKa is a dual-polarimetric radar it is capable of remotely distinguishing different hydrometeor types, and therefore microphysical processes, over large volumes of space. This study capitalizes on this capability by applying the NCAR particle identification algorithm (PID) [*Vivekanandan el al.,* 1999] to identify the most likely dominant hydrometeor within each volume of space observed by the radar. Focusing on mature MCSs observed during the active stage of the MJO, we use the radial velocity and PID fields to develop conceptual models that illustrate where hydrometeors, and their associated microphysical processes, are located with respect to the airflow features in mature MCSs that occur in the central Indian Ocean during the active stage of the MJO.

To achieve this result, we apply a spatial compositing technique to show where the different hydrometeor types, identified by the PID algorithm, are located with respect to the convective updraft and stratiform midlevel inflow layers in MCSs. While every MCS does not contain every hydrometeor type, the conceptual models presented in Figures 8 and 11 show where these hydrometeors are located if they are present. These conceptual models only depict which hydrometeor type dominates the radar signal. Smaller hydrometeors or particles with a lower dielectric constant or lower density are likely present but are not represented in our conceptual models. In mature convective updraft regions we find that:

- The convective core is characterized by MR at low levels and DA aloft. DA are the most prevalent hydrometeor above the melting level, as expected since the turbulent upper portions of a convective cell favor aggregation.
- The heaviest rain and G/RA occur just behind and below the convective core. These are likely associated with the convective-scale downdraft, whose outflow converges near the ocean surface with the updraft inflow channel. G/RA particles occur in narrow zones that extend just a few kilometers above the melting level. This structure is expected since the updrafts of tropical oceanic convective cells are not especially intense, and these large, heavy hydrometeors rapidly melt and fall to the surface upon exiting the sloping convective updraft.
- The PID never identified hail at any level in this dataset; the updrafts over tropical oceans are not large enough to produce hail particles that could survive in temperatures above freezing.

- The melting level of a convective region is sometimes marked by a band of WA, probably produced where smaller-scale vertical motions embedded within the updraft layer are locally weaker or downward (not resolved in this dataset).
- The edges of the convective region are often characterized by decreased rain intensity and SI.

Mature stratiform regions in DYNAMO/AMIE were associated with two types of MCSs. In some mature MCSs, convection sporadically entered, intensified, and collapsed within the stratiform region. In other mature MCSs, the stratiform region was located behind a rapidly propagating convective line. Despite these morphological differences, both types are associated with midlevel inflow layers and have the same systematic hydrometeor patterns relative to the midlevel inflow layer.

- The rain intensity systematically decreases toward the anvil. Most of the rain is light, some is moderate, but HR is rare and tends to only occur if the midlevel inflow reaches the surface. These patterns are expected since the stratiform updraft is unable to suspend heavier particles or allow large, heavy particles to be advected over large horizontal distances.
- Ice hydrometeors occur in well-defined layers, with a vertically thin but robust band of WA at the melting level, a thick layer of DA above the melting zone, and finally SI at the highest levels. This general layering is expected since most of the stratiform region has weak vertical air motion, allowing particles to gravitationally settle [*Houze*, 1997].
- Pockets of G/RA occur intermittently with small-scale spatial variability just above the WA layer. Stratiform regions may contain rimed particles as a result of collapsing deep convective cores [*Houze*, 1997] or small, localized convection embedded within the

mesoscale stratiform updraft that is associated with internal Kelvin-Helmholtz instability [*Hogan et al.*, 2002; *Houze and Medina*, 2005]. We cannot determine which of these riming mechanisms is acting in the RHIs examined in this study. However, comparison with the overall dataset of DYNAMO/AMIE (presented in *Rowe and Houze* [2014]) suggests that these pockets of riming occur primarily when the stratiform midlevel inflow layer is most robust.

- Small regions of HI are occasionally embedded within the stratiform region and are likely associated with enhanced dendritic growth by vapor deposition. Comparison with the overall dataset of DYNAMO/AMIE (presented in *Rowe and Houze* [2014]) indicates that this zone is most prominent when the stratiform midlevel inflow layer is robust.

The systematic hydrometeor structure within stratiform regions, regardless of whether or not the MCS is part of a leading-line/trailing stratiform MCS, is expected. Stratiform regions may occur as a result of convection either dying out to form and/or become part of a pre-existing stratiform region or being sheared off of a leading line [*Houze* 2014, Chapter 6]. In either case, the stratiform cloud is composed of old convective material whose air is still somewhat buoyant and contains particles formed in active convection. The ice particles continue to grow in the stratiform region by vapor deposition as a result of the weak residual buoyancy of the previously convective parent air parcels. Thus, the origins of stratiform precipitation are similar despite the nature of the arrangement of cells. There is therefore no a priori reason to expect the microphysics of the stratiform regions to be different between MCSs associated with leading lines or not. This similarity implies that the structure of latent heating is fundamentally similar in all stratiform regions. Further research is necessary, but this study suggests that only one latent heating parameterization should adequately describe all stratiform regions.

Several of features of the hydrometeor structure presented in this study have been observed in previous studies. For example, moderate rain is commonly observed within the convective updraft [e.g. *Jung et al.,* 2012; *Wang and Carey*; 2005; *Evaristo et al.,* 2010], frozen hydrometeors routinely have a layered structure in stratiform regions [e.g. *Houze and Churchill,* 1987, *Park et al.,* 2009; *Bechini et al.,* 2013; *Jung et al.,* 2012], and graupel is occasionally observed along the melting level of mature stratiform regions [e.g. *Takahashi and Kuhara,* 1992; *Hogan et al., 2002; Evaristo et al.,* 2010; *Rowe and Houze*, 2013, *Martini and Viltard,* 2014]. Given that the kinematic structure of mature MCSs is similar throughout the globe [e.g. *Zipser,* 1977; *Keenan and Carbone,* 1992; *LeMone et al.,* 1998], we expect mature MCSs in other geographic regions to have somewhat similar hydrometeor structure. However, some important hydrometeor differences exist between continental and tropical MCSs due to differences in the thermodynamic profile, aerosol content, and convective intensity likely [e.g. *Zipser and LeMone*, 1980; *LeMone and Zipser*, 1980]. For example, it is known that tropical West African MCSs have more graupel and possibly hail, probably because of the greater buoyancy and stronger updrafts generated over land [*Evaristo et al.*, 2010; *Cetrone and Houze*, 2011; *Yuan et al*., 2011]. Additionally, *Houze* [1989] showed that the convective regions of mesoscale systems have different vertical velocity profiles in different tropical oceanic regions. Thus, the current study describes the hydrometeor organization in MCSs in the central Indian Ocean but is not necessarily representative of all the MCSs observed globally.

While the current study focuses on mature MCSs during the active stage of the MJO during DYNAMO/AMIE, we identified five convective and two midlevel inflow RHIs during the suppressed stage and conducted the same analysis (not shown). While the representativeness of these suppressed composites is limited by their small sample size, they are qualitatively similar

to the active stage composites discussed above. This similarity between the active and suppressed stage of the MJO is consistent with *Rowe and Houze* [2014]. These results suggest that the MJO provides the large-scale environment that favors the development of MCSs but does not fundamental change the hydrometeor structure of MCSs. Thus, the kinematic structure of a MCS is a strong hydrometeor organization mechanism.

Other studies have penetrated more deeply into the microphysical structure of convection by relating dual-polarimetric observations to combinations of microphysical and electromagnetic models [*Kumjian and Ryzhkov*, 2010, 2012; *Kumjian et al.*, 2012a, 2012b, *Andrić et al.,* 2013]. Even though we use the methodology of *Vivekanandan et al.* [1999] to analyze the hydrometeor structure of mature MCSs, these hydrometeor classifications can be interpreted in terms of microphysical processes. For example, G/RA are associated with riming, DA are associated with ice particle aggregation, and WA represent melting particles.

The ability to interpret the PID in terms of microphysical processes allows the conceptual models shown in Figures 8 and 11 to be used to validate numerical simulations using generally available bin and bulk microphysical schemes in high-resolution regional and cloud-resolving models. While the conceptual models presented in the current study are not able to verify the amount and time tendency of different hydrometeor types, these conceptual diagrams will be able to verify whether or not the spatial organization of microphysical processes are accurate in relation to the mesoscale air motion patterns. The first step in conducting such a comparison is to associate each of the eight PID hydrometeor types with the hydrometeor types or microphysical processes used in numerical simulations. The association between the PID and simulated hydrometeor types is coarse. Assuming that the hydrometeors classified by the PID are precipitating, the PID categories cannot be used to verify simulated cloud water or ice, which are

usually considered to be non-precipitating. HI, SI, and DA are all represented as snow in numerical simulations. G/RA and graupel in the simulation are comparable. Given that the simulated hydrometeors instantaneously melt upon reaching the melting level, the simulated melting level should be at the same height as the top of the WA layer. Simulated rain represents WA, HR, MR, and LR. A more effective way to compare PID data to numerical simulations is in terms of microphysical processes. Instead of outputting maps of hydrometeor type, the numerical simulation can be modified to output maps of microphysical processes. Then, DA represents simulated aggregation, G/RA are comparable to simulated riming, and WA represents the simulated melting. It is important to acknowledge that the comparisons stated above are only a general reference, each parameterization scheme has a slightly different set of hydrometeor definitions and needs to be individually evaluated to ensure that the proper hydrometeors and microphysical processes are being compared. Numerical simulation/radar comparisons are a subject of ongoing research by the authors.

Acknowledgements

This research was supported by National Science Foundation grant AGS-1059611 & AGS-1355567 and Department of Energy grant DE-SC0008452 / ER-65460. The authors would like to thank NCAR S-PolKa team for collecting and quality controlling the radar and PID data, Stacy Brodzik for managing the data, Beth Tully for improving the figures, and Angela Rowe for providing helpful comments. We would also like to acknowledge Alain Protat and two anonymous reviewers for their constructive criticism that helped improve this manuscript.

References

Andrić, J., Kumjian, M. R., Zrnić, D. S., Straka, J. M., and V. M. Melnikov (2013), Polarimetric signatures above the melting layer in winter storms: An observational and modeling study, *J. Appl. Meteor.*, 52(3), 682-700.

Aydin, K. and T. A. Seliga (1984), Radar polarimetric backscattering properties of conical graupel, *J. Atmos. Sci.*, 41(11) 1887-1892.

Bader, M. J., Clough, S. A., and G. P. Cox (1987), Aircraft and dual-polarization radar observations of hydrometeors in light stratiform precipitation, *Quart. J. Roy. Meteor. Soc.*, 113(476), 491-515.

Bechini, R., Baldini, L., and V. Chandrasekar (2013), Polarimetric radar observations in the ice region of precipitating clouds at C-band and X-band radar frequencies, *J. Appl. Meteor.*, 52(5), 1147-1169.

Bouniol, D., Delanoë, J., Duroure, C., Protat, A., Giraud, V., and G. Penide (2010), Microphysical characterization of West African MCS anvils, *Quart. J. Roy. Meteor. Soc.*, 136(s1), 323-344.

Brandes, E. A., and K. Ikeda (2004), Freezing-level estimation with polarimetric radar, *J. Appl. Meteor.*, 43(11), 1541-1553.

Bringi, V. N. and V. Chandrasekar (2001), *Polarimetric Doppler Weather Radar Principles and Applications*, 636 pp., Cambridge Univ. Press, New York.

Cetrone, J., and R. A. Houze, Jr. (2011), Leading and trailing anvil clouds of West African squall lines. *J. Atmos. Sci.*, 68(5), 1114-1123.

Chen, S. S., Houze, R. A., Jr., and B. E. Mapes (1996), Multiscale variability of deep convection in relation to large-scale circulation in TOGA COARE.*J. Atmos. Sci.*, 53(10), 1380-1409.

Ciesielski, P. E., Yu, H., Johnson, R.H., Yoneyama, K., Katsumata, M., Long, C. N., Wang, J. H., Loehrer, S. M., Young, K., Williams, S. F., Brown, W., Braun, J., and T. Van Hove (2014), Quality-controlled upper-air sounding dataset for DYNAMO/AMIE/CINDY: Development and corrections, *J. Atmos. Oceanic Technol.*, 31(4), 741-764.

Dolan, B., and S. A. Rutledge (2009), A theory-based hydrometeor identification algorithm for X-band polarimetric radars, *J. Atmos. Oceanic Technol.*, 26(10), 2071-2088.

Dolan, B., Rutledge, S. A., Lim, S., Chandrasekar, V., and M. Thurai (2013), A robust C-band hydrometeor identification algorithm and application to a long-term polarimetric radar dataset, *J. Atmos. Oceanic Technol.*, 52(9), 2162-2186.

Evaristo, R., Scialom, G., Viltard, N., and Y. Lemaitre (2010), Polarimetric signatures and hydrometeor classification of West African squall lines, *Quart. J. Roy. Meteor. Soc.*, 136, 272-288, doi:10.1002/qj.561.

Hobbs, P. V. (1974), *Ice Physics*, 837 pp., Oxford Press, Bristol.

Hogan, R. J., Field, P. R., Illingworth, A. J., Cotton, R. J., and T. W. Choularton (2002), Properties of embedded convection in warm-frontal mixed-phase cloud from aircraft and polarimetric radar, *Quart. J. Roy. Meteor. Soc.*, 128(580), 451-476.

Höller, H., Bringi, V. N., Hubbert, J., Hagen, M., and P. F. Meischner (1994), Life-cycle and precipitation formation in a hybrid-type hailstorm revealed by polarimetric and Doppler radar measurements, *J. Atmos. Sci.*, 51(17), 2500-2522.

Houser, J. L., and H. B. Bluestein (2011), Polarimetric Doppler radar observations of Kelvin-Helmholtz waves in a winter storm, *J. Atmos. Sci.*, 68(8), 1676-1702.

Houze, R. A., Jr (1989), Observed stracture of mesoscale convective systems and implications for large-scale heating, *Quart. J. Roy. Meteor. Soc.*, 115(487), 425-461.

Houze, R. A., Jr (1997), Stratiform precipitation in regions of convection: A meteorological paradox? *Bull. Amer. Meteor. Soc.*, 78(10), 2179-2196.

Houze, R. A., Jr (2004), Mesoscale convective systems, *Rev. Geophys*., 42(4), doi: 10.029/2004RG0000150, 43pp.

Houze, R, A., Jr., (2014), *Cloud Dynamics*, 432 pp., Academic Press/Elsevier, Amsterdam.

Houze, R. A., Jr, and A. K. Betts (1981), Convection in GATE, *Rev. Geophys*., 19(4), 541-576.

Houze, R. A., Jr, Chen, S. S., Kingsmill, D. E., Serra, Y., and S. E. Yuter (2000), *Convection over the Pacific warm pool in relation to the atmospheric Kelvin-Rossby wave*, 57(18), 3058-3089.

Houze, R. A., Jr., and D. D. Churchill (1987), Mesoscale organization and cloud microphysics in a Bay of Bengal depression, *J. Atmos. Sci.*, 44(14), 1845-1867.

Houze, R. A., Jr., and S. Medina (2005), Turbulence as a mechanism for orographic precipitation enhancement, *J. Atmos. Sci.*, 62(10), 3599-3623.

Jung S. A., Lee, D. I., Jou, B. J. D., and H. Uyeda (2012), Microphysical properties of maritime squall line observed on June 2, 2008 in Taiwan, *J. Meteor. Soc. Japan*, 90(5), 833-850.

Keenan, T. D., and R. E. Carbone (1992), A preliminary morphology of precipitation systems in tropical northern Australia, *Quart. J. Roy. Meteor. Soc.*, 118(504), 283-326.

Kingsmill, D. E., and R. A. Houze Jr (1999a), Kinematic characteristics of air flowing into and out of precipitating convection over the west pacific warm pool: An airborne Doppler radar survey, *Quart. J. Roy. Meteor. Soc.*, 125(556), 1165-1207.

Kumjian, M. R., and A. V. Ryzhkov (2010), The impact of evaporation on polarimetric characteristics of rain: Theoretical model and practical implications, *J. Appl. Meteor.*, 49(6), 1247-1267.

Kumjian, M. R., and A. V. Ryzhkov (2012), The impact of size sorting on the polarimetric radar variables, *J. Atmos. Sci.*, 69(6), 2042-2060.

Kumjian, M. R., Ganson, S. M., and A. V. Rzyhkov (2012b), Freezing of raindrops in deep convective updrafts: A microphysical and polarimetric model, *J. Atmos. Sci.*, 69(12), 3471-3490.

Kumjian, M. R., Ryzhkov, A. V., Trömel, S., and C. Simmer (2012a), Taking the microphysical fingerprints of storms with dual-polarization radar, paper presented at 7th European Conference on Radar in Meteorology and Hydrology, Toulouse, France.

Leary, C. A., and R. A. Houze, Jr. (1979a), Structure and evolution of convection in a tropical cloud cluster, *J. Atmos. Sci.*, 36(3), 437-457.

Leary, C. A., and R. A. Houze Jr. (1979b), Melting and evaporation of hydrometeors in precipitation from the anvil clouds of deep tropical convection, *J. Atmos. Sci.*, 36(4), 669-679.

LeMone, M. A., Zipser, E. J., and S. B. Trier (1998), The role of environmental shear and thermodynamic conditions in determining the structure and evolution of mesoscale convective systems during TOGA COARE, *J. Atmos. Sci.*, 55(23), 3493-3518.

LeMone, M. A., and E. J. Zipser (1980), Cumulonimbus vertical velocity events in GATE. Part I: Diameter, intensity, and mass flux, *J. Atmos. Sci.*, 37(11), 2444-2457.

Mason, B. J. (1971), *The Physics of Clouds*, 2nd ed., 671pp., Clarendon Press, Oxford.

Martini, A., and N. Viltard (2014), Characterization of the microphysics of ice in tropical convection, paper presented at the 31st Conference on Hurricanes and tropical Meteorology, San Diego, CA.

Miles, J. W., and L. N. Howard (1964), Note on a heterogeneous shear flow, *J. Fluid Mec.*, 20(2), 331-336.

Moncrieff, M (1992), Organized convective systems: Archetypal dynamical models, mass and momentum flux theory, and parameterization, *Quart. J. Roy. Meteor. Soc.*, 118(507), 819-850.

Park, H., Ryzhkov, A. V., Zrnić, D. S., and K. E. Kim (2009), The hydrometeor classification algorithm for the polarimetric WSR-88D: Description and application to an MCS, *Wea. Forecasting*, 24(3), 730-748.

Powell, S. W., and R. A. Houze Jr. (2013), The cloud population and onset of the Madden-Julian Oscillation over the Indian Ocean during DYNAMO-AMIE, *J. Geophys. Res. Atmos.*, 118(21), 11979-11995.

Rotunno, R., Klemp, J. B., and M. L. Weisman (1988), A theory for strong, long-lived squall lines, *J. Atmos. Sci.*, 45(3), 463-485.

Rowe, A. K., and R. A. Houze Jr. (2014), Microphysical characteristics of MJO convection over the Indian Ocean during DYNAMO/AMIE, *J. Geophys. Res. Atmos.*, 119(5), 2543-2554.

Straka, J. M., Zrnić, D. S., and A. V. Ryzhkov (2000), Bulk hydrometeor classification and quantification using polarimetric radar data: Synthesis of relations, *J. Appl. Meteor.*, 39(8), 1341-1372.

Suzuki, K., Shigenaga, Y., Kawano, T., and K. Yoneyama (2006), Videosonde observations during the R/V Mirai MR04-08 Cruise, *J. Mar. Meteorol. (Umi to Sora)*, 82(2), 1-10.

Takahashi, T. and K. Kuhara (1993), Precipitation mechanisms of cumulonimbus clouds at Pohnpei, Micronesia, *J. Meteor. Soc. Japan*, 71(1), 21-31.

Takahashi, T., Suzuki, K., Orita, M., Tokuno, M., and R. Delamar (1995), Videosonde observations of precipitation processes in equatorial cloud clusters, *J. Meteor. Soc. Japan*, 73(2B), 509-534.

Tessendorf, S. A., Miller, L. J., Wiens, K. C., and S. A. Rutledge (2005), The 29 June 2000 supercell observed during STEPS. Part 1: Kinematics and microphysics, *J. Atmos. Sci.*, 62(12), 4127-4150.

Vivekanandan, J., Zrnić, D. S., Ellis, S. E., Oye, R., Ryzhkov, A. V., and J. Straka (1999), Cloud microphysics retrieval using S-band dual-polarization radar measurements, *Bull. Amer. Meteor. Soc.*, 80(3), 381-387.

Wang, J. J., and L. D. Carey (2005), The development and structure of an oceanic squall-line system during the South China Sea Monsoon Experiment, *Mon. Wea. Rev.*, 133(6), 1544-1561.

Wolde, M., and G. Vali (2001a), Polarimetric signatures from ice crystals observed at 95 GHz in winter clouds. Part 1: Dependence on crystal form, *J. Atmos. Sci.*, 58(8), 828-841.

Yamada, H., Yoneyama, K., Katsumata, M., and R. Shirooka (2010), Observations of a super cloud cluster accompanied by synoptic-scale eastward-propagating precipitating systems over the Indian Ocean. *J. Atmos. Sci.*, 67(5), 1456–1473.

Yoneyama, K., Zhang, C. D., and C. N. Long (2013), Tracking pulses of the Madden-Julian Oscillation, *Bull. Amer. Meteor. Soc.*, 94(12), 1871-1891.

Yuan, J., Houze, R. A., Jr., and A. J. Heymsfield (2011), Vertical structures of anvil clouds of tropical mesoscale convective systems observed by CloudSat. *J. Atmos. Sci.*, 68(8), 1653-1674.

Zipser, E. J (1977), Mesoscale and convective-scale downdrafts as distinct components of squall-line structure, *Mon. Wea. Rev.*, 105(12), 1568-1589.

Zipser, E. J., and M. A. LeMone (1980), Cumulonimbus vertical velocity events in GATE. Part II: Synthesis and model core structure. *J. Atmos. Sci.*, 37(11), 2458-2469.

Zrnić, D. S., Balakrishnan, N., Ziegler, C. L., Bringi, V. N., Aydin, K., and T. Matejka (1993), Polarimetric signatures in the stratiform region of a mesoscale convective system, *J. Appl. Meteor.*, 32(4), 678-693.

Zuluaga, M. D., and R. A. Houze, Jr. (2013), Evolution of the population of precipitating convective systems over the equatorial Indian Ocean in active phases of the Madden-Julian Oscillation. *J. Atmos. Sci.*, 70(9), 2713-2725.

Tables

Table 1: Approximate ranges of values for hydrometeor types in PID

	Z_H (dBZ)	ZDR (dB)	L_{DR} (dB)	K_{DP} (° km^{-1})	ρ_{HV}	T (°C)
Graupel/Rimed Aggregates (G/RA)	30 - 50	-0.1 - 0.76	-25 - -20.17	0.08 - 1.65	0.89 – 0.96	-50 - 7
Graupel/Rain (G/R)	30-50	0.7 - 1	-25 - -20.17	0.1 - 1.7527	0.85 - 0.98	-25 - 7
Hail (H)	50-90	-3 - -1	-25 - -10.4	0 - 0.2	0.88 - 0.96	-50 -30
Hail/Rain (H/R)	50-90	1.4 - 5	- 27 - -25.5	1 - 5	0.86 - 0.97	-25 - 30
Heavy Rain (HR)	45 - 55	0.34 - 4.35	-31 - -24.5	0.09 – 15.55	0.97 - 0.99	1 - 40
Moderate Rain (MR)	35- 45	0.01 - 3.04	-31 - -24.8	-0.01 – 2.99	0.97 – 0.99	1 - 40
Light Rain (LR)	10 - 35	0- 1.8	-31 - -27	-0.02 – 0.26	0.97 – 0.99	1 - 40
Wet Aggregates (WA)	7 - 45	0.5 - 3	-26 - -17.2	0.1 - 1	0.75 – 0.98	-4 – 12
Dry Aggregates (DA)	15 - 33	0 - 1.1	-26 - -17.2	0 – 0.168	0.97 - -0.98	-50 - 1
Small Ice Crystals (SI)	0 - 15	0 - 0.7	-31 - -23.4	0 – 0.1	0.97 – 0.98	-50 - 1
Horizontally Oriented Ice Crystals (HI)	0 - 15	1 - 6	-31 - -23.4	0.6 - 0.8	0.97 -0.98	-50 - 1

Table 2: Width, height, and slope of convective updraft regions

Date, Time	Width (km)	Height (km)	Slope (degrees)
16 Oct, 1535 UTC	7.67	9.52	42.24
18 Oct, 1550 UTC	5.24	12.08	55.63
18 Oct, 1705 UTC	10.8	15.15	40.7
20 Oct, 0135 UTC	2.7	10.58	67.15
20 Oct, 1605 UTC	9.44	13.62	43.36
20 Oct, 2205 UTC	11.4	15.09	38.53
22 Oct, 0050 UTC	10.65	12.24	45.34
22 Oct, 0407 UTC	5.54	10.1	48.36
24 Oct, 0135 UTC	7.96	15.61	49.28
24 Oct, 0235 UTC	5.4	9.79	58.38
24 Oct, 0250 UTC	7.94	16.93	59.74
17 Nov, 1905 UTC	11.7	15.45	38.65
17 Nov, 2305 UTC	5.69	15.38	57.64
18 Nov, 0035 UTC	9.61	11.64	45.22
18 Nov, 0735 UTC	6.45	10.52	52.37
18 Nov, 0750 UTC	1.65	8.33	73.58
18 Nov, 0905 UTC	1.5	12.11	80.63
18 Nov, 1050 UTC	0.9	9.8	79.33
23 Nov, 0750 UTC	2.54	13.12	68.32
27 Nov, 0150 UTC	5.7	8.35	39.88
19 Dec, 2335 UTC	2.84	7.68	61.87
21 Dec, 0135 UTC	4.5	12.59	59.42
21 Dec, 2050 UTC	19.34	11.55	24.86
22 Dec, 2020 UTC	5.26	8.56	53.27
23 Dec, 1835 UTC	8.71	13.76	49.56

Table 3: Width, height, slope, and presence of leading convective line in stratiform midlevel inflow regions

Date, Time	Leading Line	Width (km)	Height (km)	Slope (degree)
16 Oct, 0535 UTC	No	49.8	13.76	-1.2
16 Oct, 0820 UTC	No	60.46	10.86	-3.14
16 Oct, 1320 UTC	No	28.5	8.64	-0.31
17 Oct, 2235 UTC	No	26.54	7.499	-2.96
18 Oct, 0905 UTC	No	19.8	12.63	-1.19
18 Oct, 1305 UTC	No	22.5	12.19	-0.28
18 Oct, 1835 UTC	No	21.6	11.5	-1.59
20 Oct, 1535 UTC	Yes	19.36	12.67	-3.2
20 Oct, 1935 UTC	No	15.44	12.82	-1.61
20 Oct, 2235 UTC	No	18.15	8.78	-0.99
21 Oct, 2150 UTC	No	55.34	14.57	-2.06
22 Oct, 0435 UTC	No	30.9	11.7	-2.6
22 Oct, 0750 UTC	No	24.75	9.74	-1.46
23 Oct, 2320 UTC	No	25.05	8.56	-2.5
24 Oct, 0305 UTC	No	43.04	13.38	-1.82
24 Oct, 0605 UTC	No	36.62	9.645	-0.55
24 Oct, 1950 UTC	No	10.04	7.8	-3.97
26 Oct, 0920 UTC	No	36.33	9.32	-1.21
17 Nov, 1705 UTC	No	31.04	12.94	-3.61
17 Nov, 2050 UTC	No	51.29	13.66	-0.68
18 Nov, 0150 UTC	No	38.82	13.07	-2.25
22 Nov, 1935 UTC	No	27.75	12.71	-3.98
22 Nov, 2020 UTC	No	25.8	11.02	-2.45
22 Nov, 2220 UTC	No	30.74	8.91	-1.87
23 Nov, 0050 UTC	No	31.19	13.61	-2.39
23 Nov, 0235 UTC	No	22.36	8.31	-2.77
23 Nov, 1120 UTC	No	79.04	12.33	-1.33
23 Nov, 1320 UTC	No	40.37	10.96	-0.16
26 Nov, 1150 UTC	Yes	34.5	12.71	-1.43
26 Nov, 1235 UTC	Yes	17.85	10.57	-3.3
26 Nov, 1705 UTC	No	44.1	9.51	-2.81
27 Nov, 0150 UTC	Yes	46.21	5.83	-1.6
20 Dec, 1535 UTC	Yes	47.85	10.14	-1.65
20 Dec, 1720 UTC	Yes	53.25	11.27	-2.1
23 Dec, 1705 UTC	Yes	38.7	11.95	-4.9
23 Dec, 1850 UTC	Yes	56.10	13.53	-3.55

23 Dec, 2250 UTC	Yes	31.36	11.9	-2.851055

Table 4: Median temperature, average of temperature of coldest 10%, and average temperature of warmest 10% of frozen hydrometeors.

	G/RA			WA			DA			SI			HI		
	Coldest	Warmest	Median	Coldest	Warmest	Median	Coldest	Warmest	Median	Coldest	Warmest	Median	Coldest	Warmest	Median
Convective Updraft	-12.5	0.3	-3.7	-4.9	1.1	-0.9	-46.9	-2.8	-14.3	-69	-10.3	-35.8	-62.7	-11.2	-47.4
Midlevel Inflow Without Leading Line	-4	1.7	-0.5	-2.3	1.6	0.11	-28.3	-2.3	-9.5	-58.2	-7.7	-29.9	-39.5	-9.9	-17.7
Midlevel Inflow With Leading Line	-2.9	0.79	-0.08	-2.6	1.2	-0.17	-27.5	-1.41	-10.4	-54.7	-4.6	-26.1	-18	-9.4	-15.6

1063

Table 5: Frequency of occurrence of contiguous hydrometeors regions in all RHIs

	Convective Updraft	Midlevel Inflow Without a Leading Convective Line	Midlevel Inflow With a Leading Convective Line
Graupel/Rimed Aggregates (G/RA)	88%	64%	66%
Heavy Rain (HR)	92%	14%	11%
Moderate Rain (MR)	100%	60%	55%
Light Rain (LR)	72%	100%	100%
Wet Aggregates (WA)	92%	100%	100%
Dry Aggregates (DA)	100%	100%	100%
Small Ice Crystals (SI)	92%	89%	100%
Horizontally-Oriented Ice Crystals (HI)	20%	53%	44%

Figure Captions

Figure 1: Azimuthal portion of S-PolKa domain containing high resolution RHI scans within 100 km of the radar shown in gray.

Figure 2: Schematic of airflow through the (a) convective and (b) stratiform portion of MCS over the west Pacific Ocean as observed by airborne Doppler radars during TOGA COARE. The numbers indicate the horizontal velocity of the airflow and the horizontal and vertical extent of the airflow features. The slope of the convective updraft is also indicated in (a). Figure based on *Kingsmill and Houze* [1999a].

Figure 3: Bar charts showing the distribution of (a) reflectivity, (b) differential reflectivity, (c) temperature, (d) linear depolarization ratio, (e) correlation coefficient, and (f) specific differential phase of all radar volumes in convective updraft regions and contain a contiguous region of graupel/rimed aggregates, heavy rain, moderate rain, light right, wet aggregates, dry aggregates, small ice particles, and horizontally-oriented ice crystals. The red line is the median, the blue lines are the 25% and 75% quartiles, the black lines represent 99.3% of the data, and the red stars are outliers. (g-l) Same as (a-f) except for stratiform midlevel inflow regions.

Figure 4: Vertical cross-section showing the (a) most likely dominant hydrometeor type (1st PID), (b) second most likely dominant hydrometeor type (2nd PID), and (c) the difference in their interest values for a convective updraft at 0250 UTC on 24 October 2011. The black lines outline the convective updraft region. (d-f) same as (a-c) except for a stratiform midlevel inflow region at 0150 UTC on 18 November 2011 and the black lines outline the stratiform region.

Figure 5: RHI scan showing (a) reflectivity, (b) hydrometeor type from the PID, (c) Z_{DR}, (d) K_{DP}, (e) radial velocity, (f) temperature, (g) ρ_{hv}, and (h) LDR through a convective updraft at 0250

UTC on 24 October 2011. The black line surrounds the convective updraft region. The dashed line in (b) shows the convective updraft line.

Figure 6: Same as Figure 5 except for a stratiform midlevel inflow region at 0150 UTC on 18 November 2011. The black line surrounds the stratiform region. The dashed line in (b) shows the midlevel inflow line.

Figure 7: Composites showing the location of (a) heavy rain, (b) light rain, (c) wet aggregates, (d) small ice crystals, (e) moderate rain, (f) graupel/rimed aggregates, (g) dry aggregates, and (h) horizontally-oriented ice in convective updrafts. The horizontal and vertical axes are expressed as fractions of the width and height of the convective updraft core and are referred to as the normalized width and height, respectively. The black line represents the composite convective updraft. Shading represents the frequency of each hydrometeor type at that location relative to the convective updraft. The color bar in each panel varies.

Figure 8: Schematic showing the location of hydrometeor types relative to the convective updraft. The black lines represent the convective updraft. The gray line represents the surface. The colored regions depict where each hydrometeor is most likely located relative to the convective updraft. The percentages listed in the color bar indicate the average areal coverage of each hydrometeor within convective updraft RHIs.

Figure 9: Vertical profile of reflectivity through a portion of the RHI scan in a stratiform midlevel inflow region at 0150 UTC on 18 November 2011 shown in Figure 6 that (a) contains and (c) does not contain graupel/rimed aggregates above the wet aggregate layer. The black line shows the vertical profile of reflectivity. The colored dots represent the location of each hydrometeor type. (b) and (d) same as (a) and (c) except vertical profiles of Z_{DR} are shown.

Figure 10: Same as Figure 8 except for stratiform midlevel inflow RHIs that are not associated with a leading-convective line. The black line represents the composite stratiform midlevel inflow.

Figure 11: Schematic showing the location of hydrometeor types relative to the stratiform midlevel inflow. The solid black lines in the background represent the stratiform midlevel inflow. The dashed black lines indicates the melting level. The gray line represents the surface. The colored regions depict where each hydrometeor is most likely located relative to the stratiform midlevel inflow. The percentages listed in the color bar indicate the average areal coverage of each hydrometeor within RHIs taken through stratiform midlevel inflow.

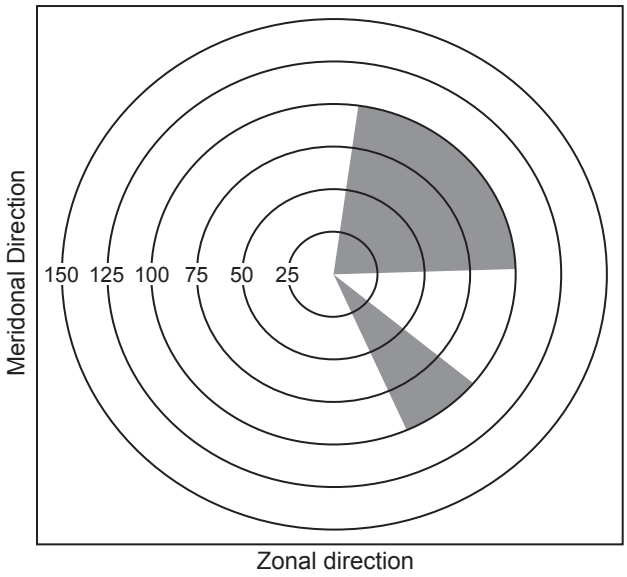


Fig. 1. Azimuthal portion of S-PolKa domain containing high resolution RHI scans within 100 km of the radar shown in gray.

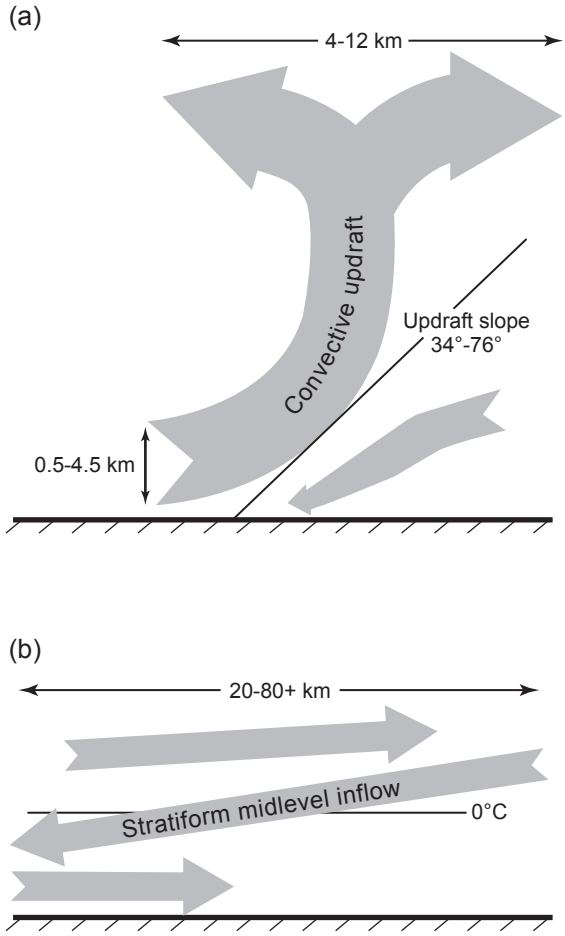


Fig. **2.** Schematic of airflow through the (a) convective and (b) stratiform portion of MCS over the west Pacific Ocean as observed by airborne Doppler radars during TOGA COARE. The numbers indicate the horizontal velocity of the airflow and the horizontal and vertical extent of the airflow features. The slope of the convective updraft is also indicated in (a). Figure based on *Kingsmill and Houze* [1999a].

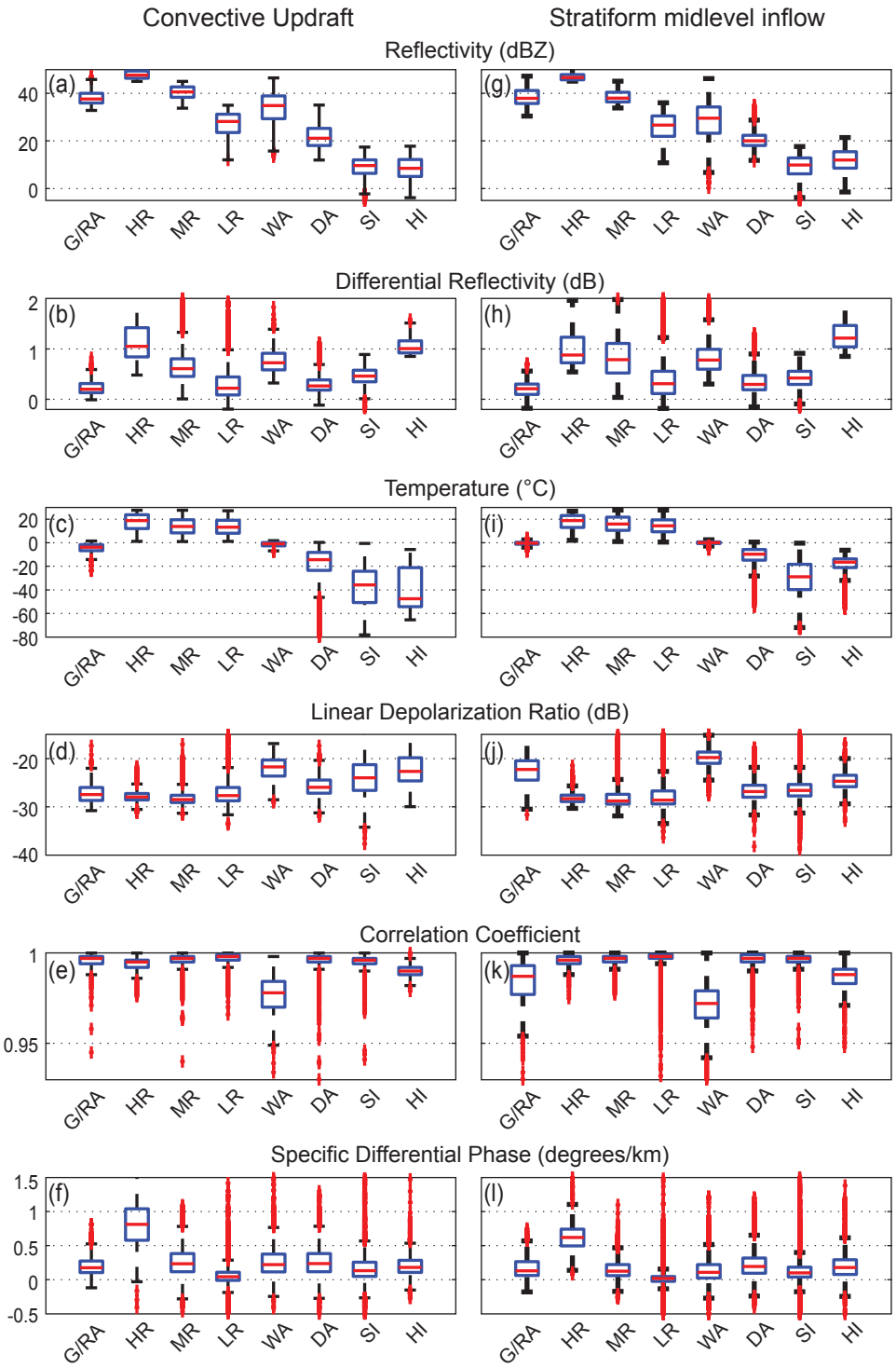


Fig. 3. Bar charts showing the distribution of (a) reflectivity, (b) differential reflectivity, (c) temperature, (d) linear depolarization ratio, (e) correlation coefficient, and (f) specific differential phase of all radar volumes in convective updraft regions and contain a contiguous region of graupel/rimed aggregates, heavy rain, moderate rain, light right, wet aggregates, dry aggregates, small ice particles, and horizontally-oriented ice crystals. The red line is the median, the blue lines are the 25% and 75% quartiles, the black lines represent 99.3% of the data, and the red stars are outliers. (g-l) Same as (a-f) except for stratiform midlevel inflow regions.

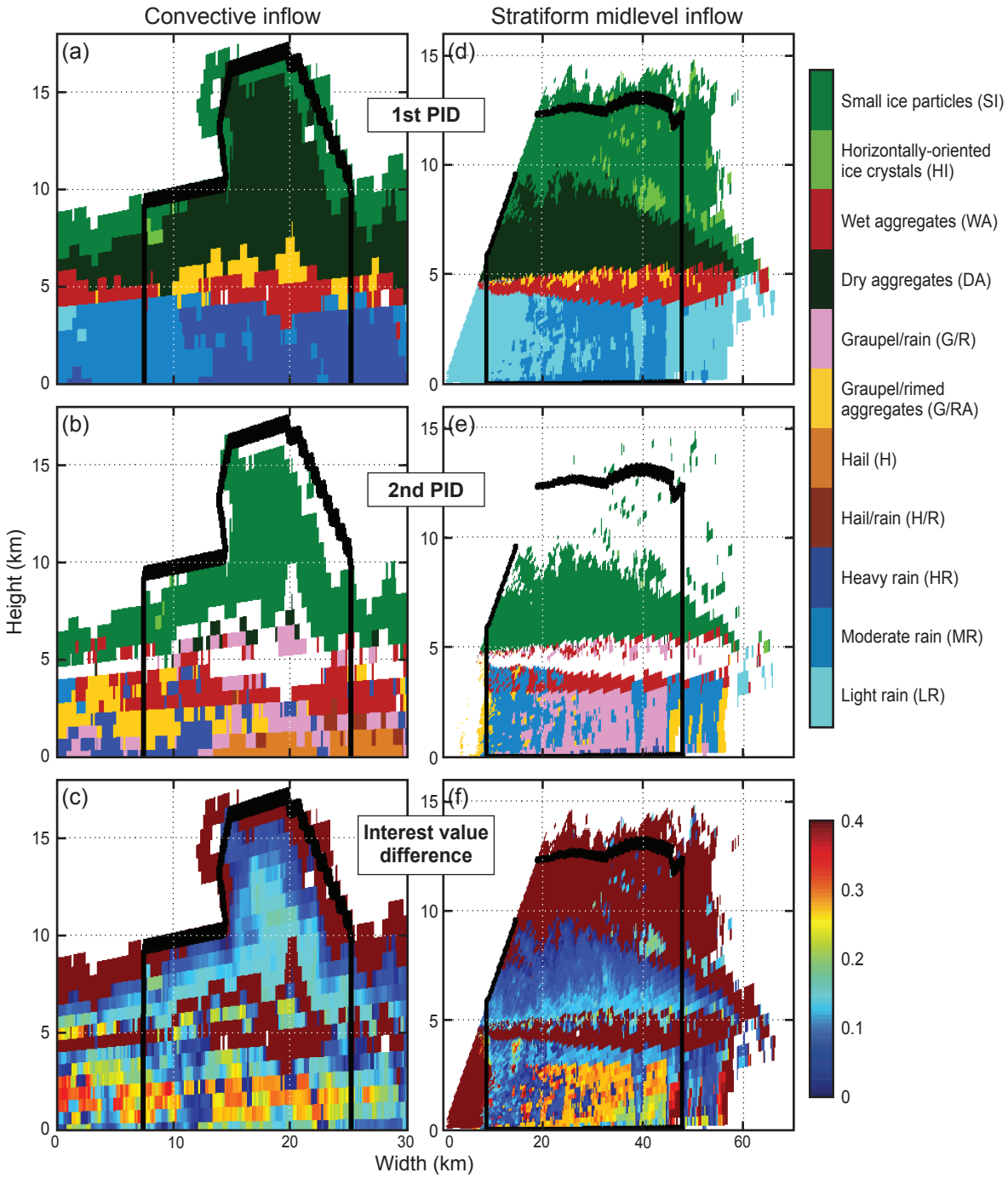


Fig. 4. Vertical cross-section showing the (a) most likely dominant hydrometeor type (1st PID), (b) second most likely dominant hydrometeor type (2nd PID), and (c) the difference in their interest values for a convective updraft at 0250 UTC on 24 October 2011. The black lines outline the convective updraft region. (d-f) same as (a-c) except for a stratiform midlevel inflow region at 0150 UTC on 18 November 2011 and the black lines outline the stratiform region.

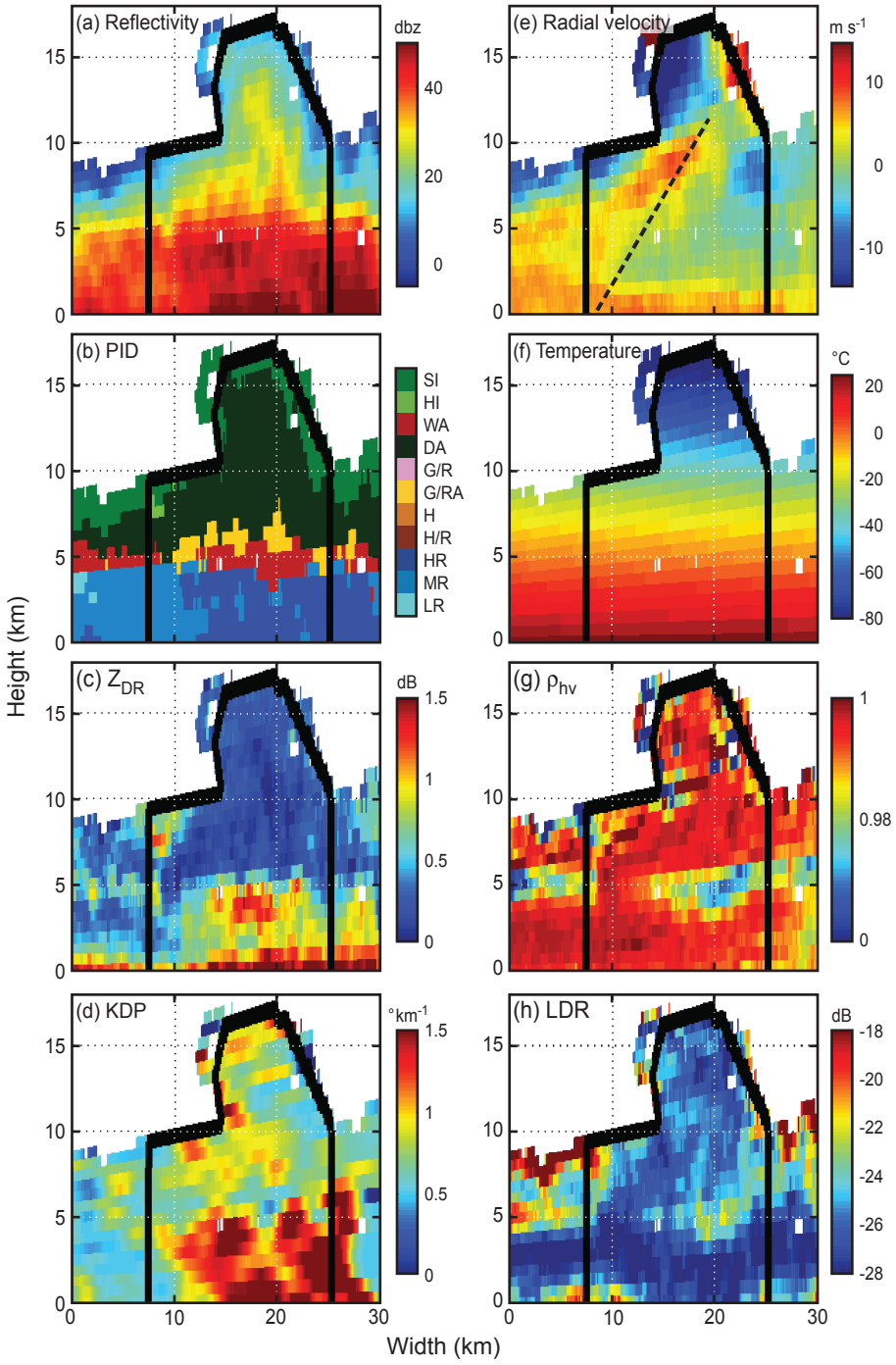


Fig. 5. RHI scan showing (a) reflectivity, (b) hydrometeor type from the PID, (c) Z_{DR}, (d) K_{DP}, (e) radial velocity, (f) temperature, (g) ρ_{hv}, and (h) LDR through a convective updraft at 0250 UTC on 24 October 2011. The black line surrounds the convective updraft region. The dashed line in (b) shows the convective updraft line.

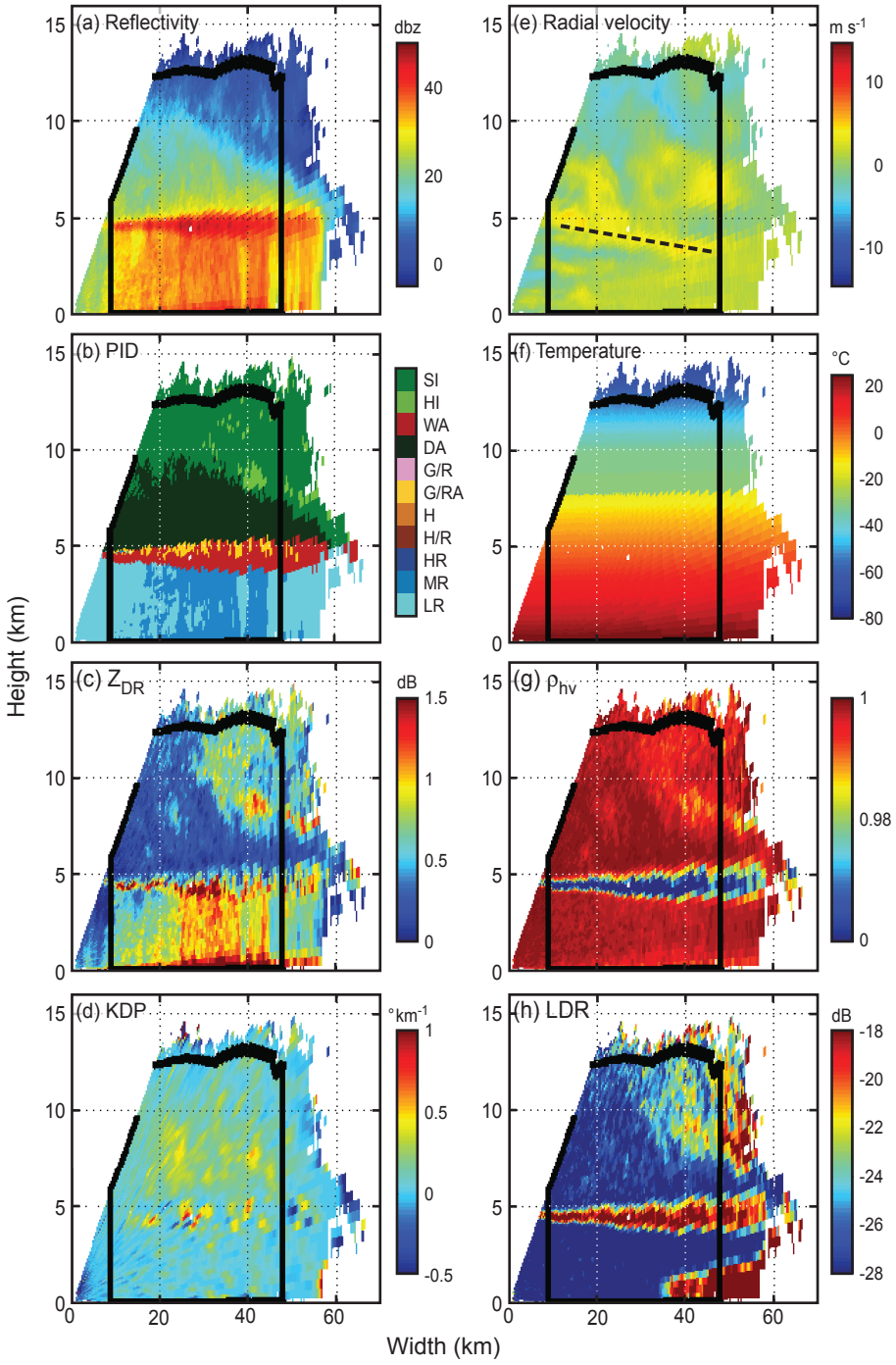


Fig. 6. Same as Figure 5 except for a stratiform midlevel inflow region at 0150 UTC on 18 November 2011. The black line surrounds the stratiform region. The dashed line in (b) shows the midlevel inflow line.

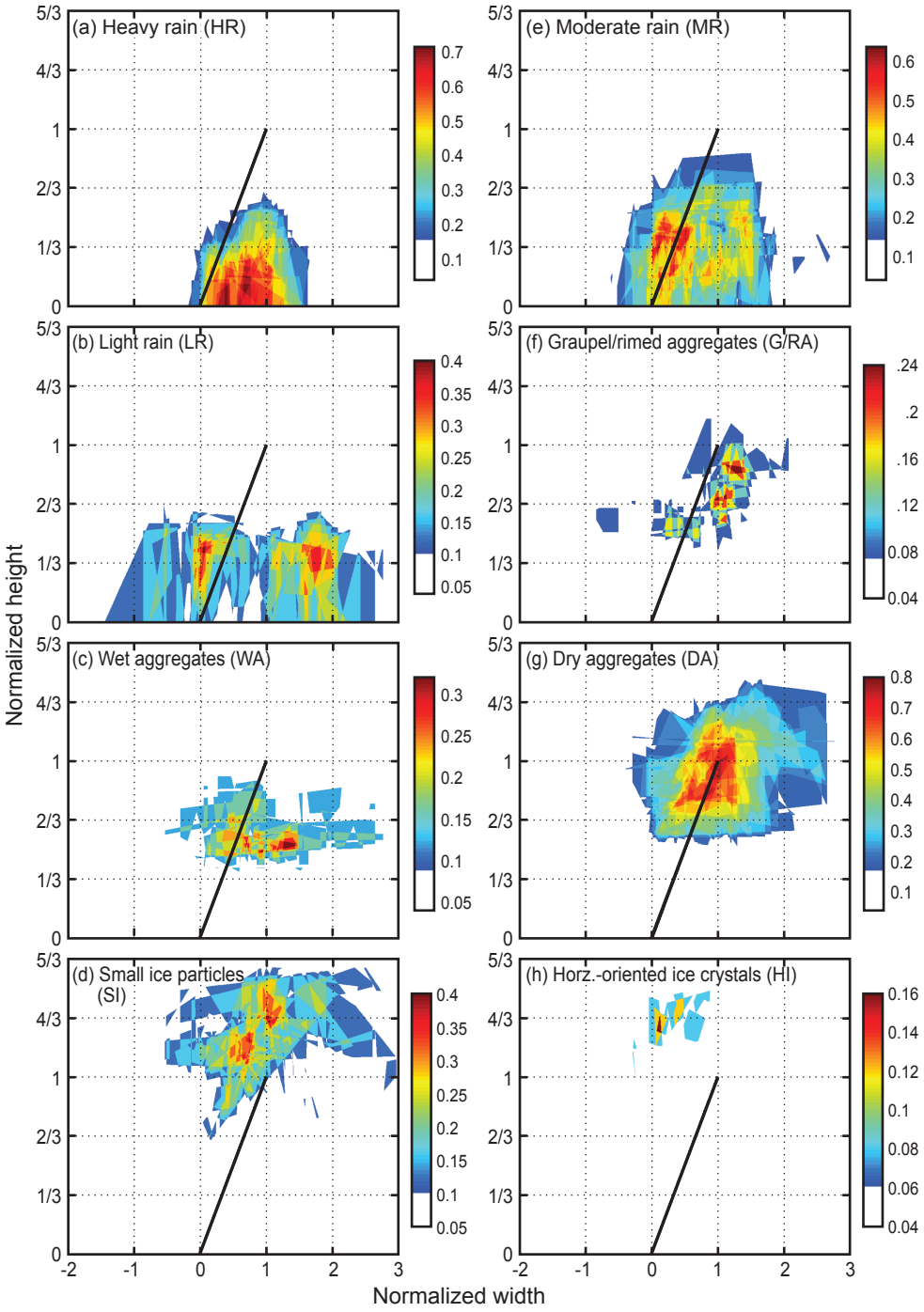


Fig. 7. Composites showing the location of (a) heavy rain, (b) light rain, (c) wet aggregates, (d) small ice crystals, (e) moderate rain, (f) graupel/rimed aggregates, (g) dry aggregates, and (h) horizontally-oriented ice in convective updrafts. The horizontal and vertical axes are expressed as fractions of the width and height of the convective updraft core and are referred to as the normalized width and height, respectively. The black line represents the composite convective updraft. Shading represents the frequency of each hydrometeor type at that location relative to the convective updraft. The color bar in each panel varies.

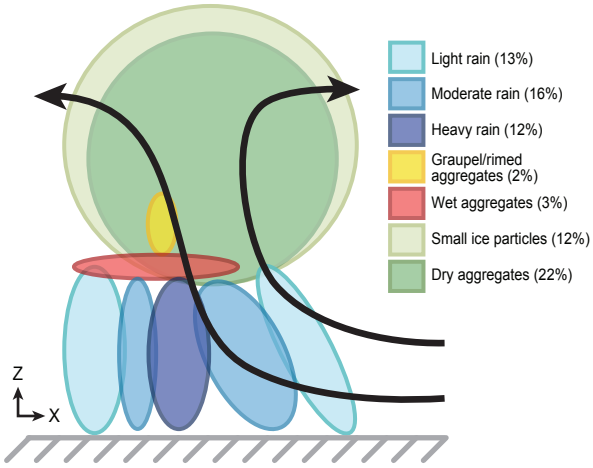


Fig. 8. Schematic showing the location of hydrometeor types relative to the convective updraft. The black lines represent the convective updraft. The gray line represents the surface. The colored regions depict where each hydrometeor is most likely located relative to the convective updraft. The percentages listed in the color bar indicate the average areal coverage of each hydrometeor within convective updraft RHIs.

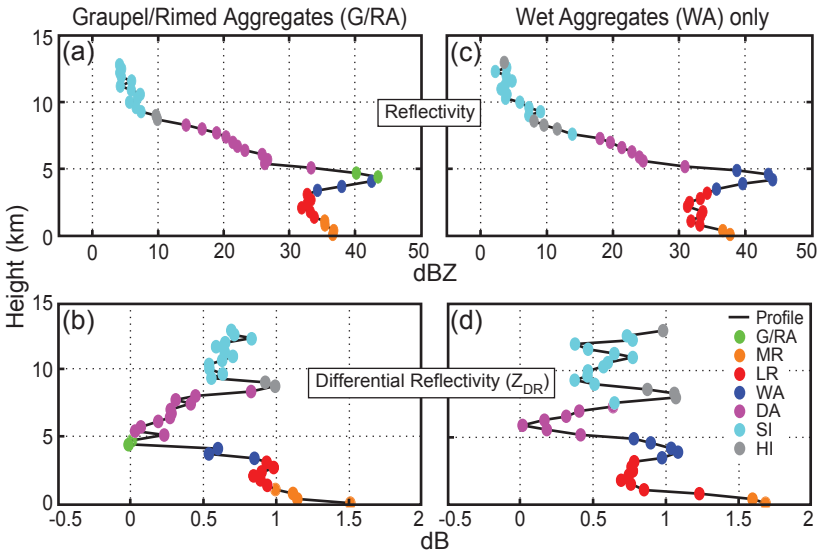


Fig. 9. Vertical profile of reflectivity through a portion of the RHI scan in a stratiform midlevel inflow region at 0150 UTC on 18 November 2011 shown in Figure 6 that (a) contains and (c) does not contain graupel/rimed aggregates above the wet aggregate layer. The black line shows the vertical profile of reflectivity. The colored dots represent the location of each hydrometeor type. (b) and (d) same as (a) and (c) except vertical profiles of Z_{DR} are shown.

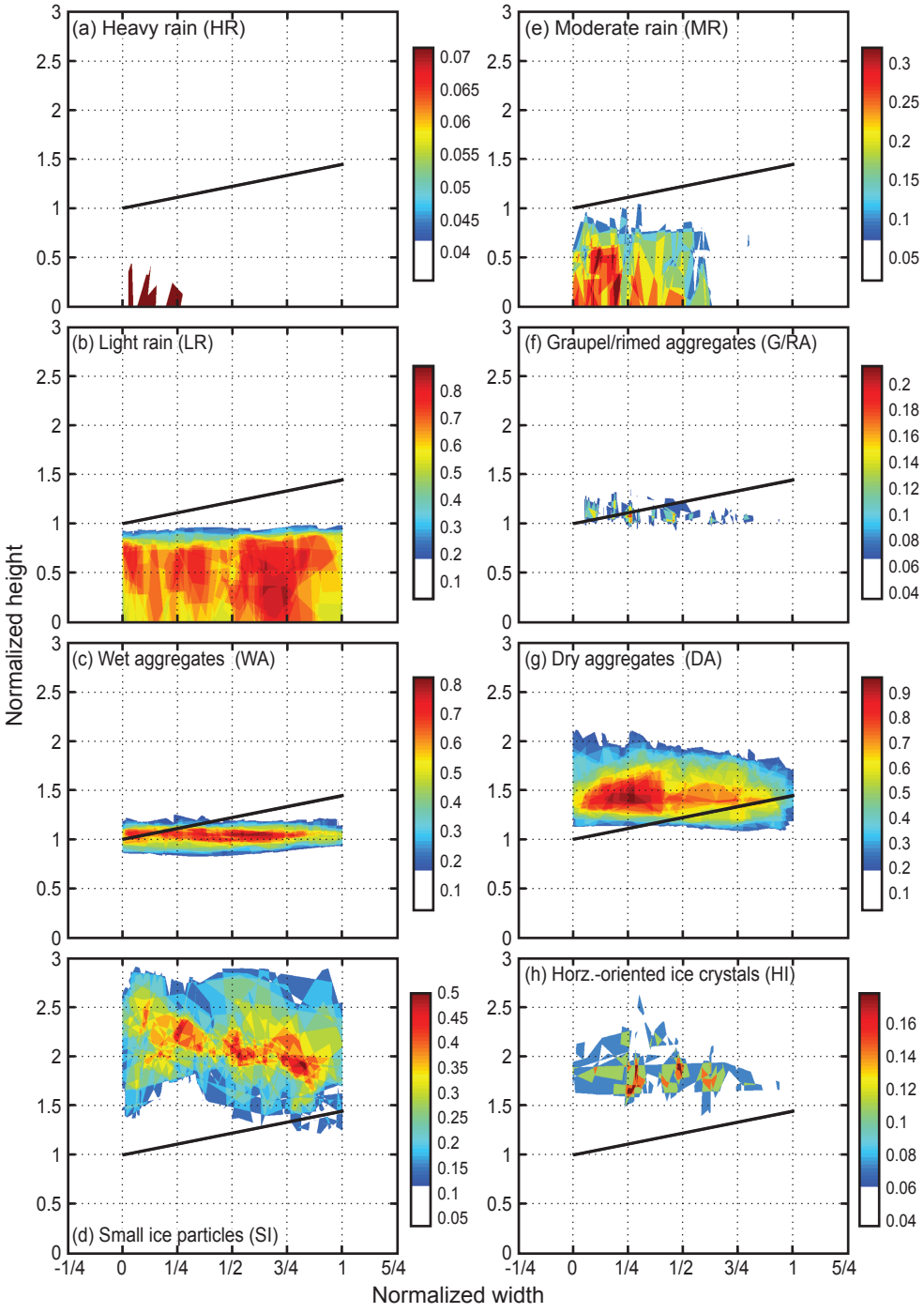


Fig. 10. Same as Figure 8 except for stratiform midlevel inflow RHIs that are not associated with a leading-convective line. The black line represents the composite stratiform midlevel inflow.

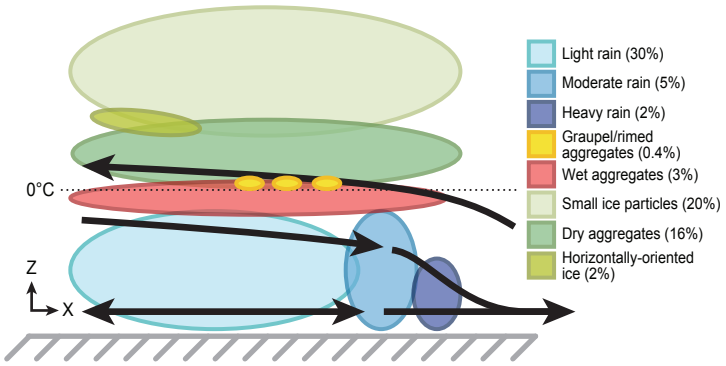


Fig. 11. Schematic showing the location of hydrometeor types relative to the stratiform midlevel inflow. The solid black lines in the background represent the stratiform midlevel inflow. The dashed black lines indicates the melting level. The gray line represents the surface. The colored regions depict where each hydrometeor is most likely located relative to the stratiform midlevel inflow. The percentages listed in the color bar indicate the average areal coverage of each hydrometeor within RHIs taken through stratiform midlevel inflow.